AMERICAN UNIVERSITY OF BEIRUT

IMPACT OF THE COSMIC MAGNETIC FIELD ON THE FORMATION OF THE EARLY STARS IN THE UNIVERSE

by
CYNTHIA RAYMOND SAAD

A thesis
submitted in partial fulfillment of the requirements
for the degree of Doctor of Philosophy
to the Department of Physics
of the Faculty of Arts and Sciences
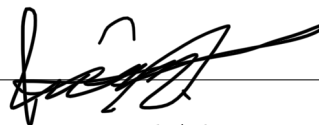at the American University of Beirut

Beirut, Lebanon
October 2022

AMERICAN UNIVERSITY OF BEIRUT

Impact of the cosmic magnetic field on the formation of the early stars in the Universe

by
CYNTHIA RAYMOND SAAD

Approved by:

_____

Dr. Jihad Touma, Professor   Departmental Advisor

Physics

_____

Dr. Leonid Klushin, Professor   Member of Committee (chair)

Physics

_____

Dr. Issam Lakkis, Professor   Member of Committee

Mechanical Engineering

_____

Dr. Volker Bromm, Professor   Member of Committee

University of Texas at Austin, USA

_____

Dr. John Wise, Associate Professor   Member of Committee

Center for Relativistic Astrophysics, Georgia Tech

Date of thesis defense: October 27, 2022

AMERICAN UNIVERSITY OF BEIRUT

THESIS RELEASE FORM

Student Name: _____Saad_____Cynthia_____Raymond_____
          Last   First   Middle

I authorize the American University of Beirut, to: (a) reproduce hard or electronic copies of my thesis; (b) include such copies in the archives and digital repositories of the University; and (c) make freely available such copies to third parties for research or educational purposes:

[X] As of the date of submission

[ ] One year from the date of submission of my thesis.

[ ] Two years from the date of submission of my thesis.

[ ] Three years from the date of submission of my thesis.

_____   ___November 21, 2022___
Signature   Date

(This form is signed & dated when submitting the thesis to the University Libraries ScholarWorks)

ACKNOWLEDGEMENTS

Abstract

of the Thesis of

Cynthia Raymond Saad   for   Doctor of Philosophy
                                          Major: Physics

Title: Impact of the cosmic magnetic field on the formation of the early stars in the Universe

The investigation of the formation of the first stars in the Universe, termed Population III (Pop III), has until now largely neglected the impact of the cosmic magnetic field on their formation. Our present work focuses on the fragmentation properties of primordial protostellar discs and how they are modified by including magneto-hydrodynamic (MHD) aspects. We start from cosmological initial conditions at $z = 100$, then analyse the dynamics inside the most massive minihalo at a redshift close to $z \sim 25$. A magnetic field is inserted at an intermediate evolutionary stage, normalized to a fraction of the equipartition value. In order to explore the parameter space, different magnetic field geometries are considered including uniform, radial, toroidal, and poloidal configurations. The collapse of the gas is followed for ~ 8 orders of magnitude in density after the field was inserted, until a maximum of $10^{15}\,\mathrm{cm}^{-3}$ is reached. We find that the magnetic field leads to a delay in the collapse of the gas and inhibits the fragmentation of the emerging disc surrounding the central core. Moreover, the geometry of the field affects the collapse and the multiplicity of Pop III stars. The full understanding of the formation of these stars and their mass distribution thus needs to take into account the effect of magnetic fields. We further conclude that ideal MHD is only a first step in this endeavor, to be followed-up with a comprehensive treatment of dissipative effects, such as ambipolar diffusion and Ohmic dissipation. This is worth doing in future works.

TABLE OF CONTENTS

ILLUSTRATIONS

TABLES

ABBREVIATIONS

CDM	Cold Dark Matter
CMB	Cosmic Microwave Background
EGMF	Extragalactic magnetic fields
EMP	Extremely metal-poor
GRB	Gamma ray burst
IGM	Intergalactic medium
IMF	Initial mass function
PMF	Primordial magnetic field
Pop III	Population III stars
Rand	Random magnetic field configuration
PI	Poloidal magnetic field with Intermediate magnitude
PL	Poloidal magnetic field with Low magnitude
PH	Poloidal magnetic field with High magnitude
RI	Radial magnetic field with Intermediate magnitude
RL	Radial magnetic field with Low magnitude
RH	Radial magnetic field with High magnitude
TI	Toroidal magnetic field with Intermediate magnitude
TL	Toloidal magnetic field with Low magnitude
TH	Toloidal magnetic field with High magnitude
UFD	Ultra-faint dwarf
UI	Uniform magnetic field with Intermediate magnitude
UL	Uniform magnetic field with Low magnitude
UMP	Ultra metal-poor
UH	Uniform magnetic field with High magnitude

CHAPTER 1

INTRODUCTION

The formation of the first stars in the universe has a crucial relation to cosmology. As we will see in the present thesis work, the initial conditions of their formation are given according to the cosmological dark matter model (Briefly: ΛCDM). The formation of these stars classified as Pop III stars is thought to have ended epoch of the so called "cosmic dark age", which is the time interval following the recombination time 380000 years after big bang, where the cosmic gas became neutral and decoupled from the photons. During the dark age, the background was filled with infrared radiation (see Fig. 1.1) the remnant of the primordial fire ball. The expansion of the universe has shifted the infrared radiation to the cosmic microwave background radiation (CMB) we observe in the present-day universe.

The metaphor "dark age" is somewhat misleading because it assumes a hypothetical observer to see visible light. The visible light came back after the formation of the first stars in the universe, the Pop III stars which have reionized the universe through their ultraviolet light.

Till recently, the dark age period was estimated to be about 400 million years after recombination. However, new radio observation by [1] with an absorption profile centered at 78 MHz revealed a dark age of only about 180 million years. This finding is based on the view that the ultraviolet light has penetrated the primordial hydrogen gas and altered the excitation state of its 21-cm hyperfine line. This alteration allows the gas to absorb photons from the cosmic microwave, which expects to produce a spectral distortion that can be observed today at radio frequency less than 200 MHz. The observations by [1] yielded a flattened absorption profile centered at 78 MHz and is consistent with expectations for the 21-cm signal induced by early stars. The conclusion from this observation is that stars existed around 180 million years after big bang. Furthermore, the absorption profile was found centered at redshift $z = 17$ and span a range $20 \leq z \leq 15$.

The formation of Pop III stars is distinct from contemporary star formation. The difference is summarized as follows:
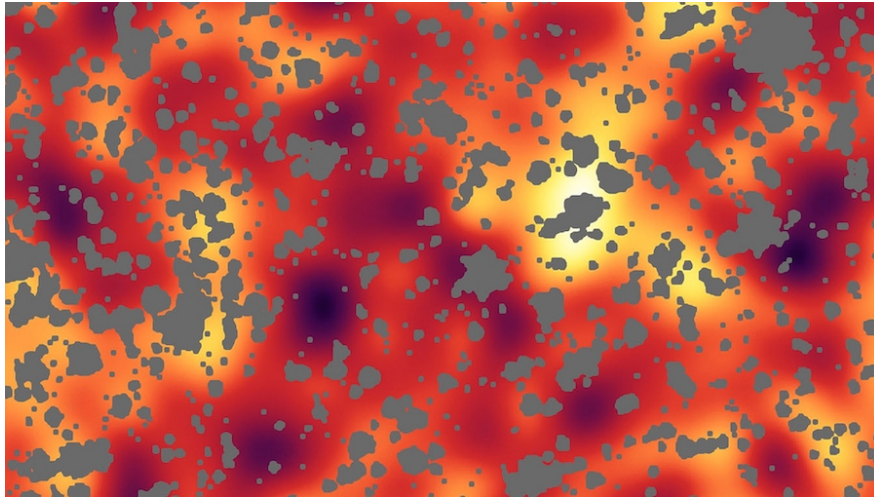
Figure 1.1: This image from NASA's Spitzer Space Telescope shows infrared light originated from the first luminous objects, which emerged at the end of the so-called "Dark Ages". After masking out all known stars corresponding to the gray blobs, the light of these early stars and black holes is revealed by the brighter areas. **Credits: NASA/JPL-Caltech/A. Kashlinsky (Goddard)**

1. They could not have elements or isotopes heavier than Lithium, since it is established (e.g., [2] and references therein) that the primordial nucleosynthesis cannot lead to elements like carbon and above. This is termed as zero metallicity.

2. They are believed to be very massive and luminous stars. During their lifetime, they formed the heavy metals and ionized gas around them with their ultraviolet light. Their final evolutionary stages were violent supernovae explosions that enriched the primordial gas with the first heavy elements in the universe.

3. The Pop III star formation is simpler in terms of chemistry and radiation feedback from other not yet existing structure. Also, the initial conditions for the formation of such stars are well defined and set by cosmological models namely model calibrated to high precision by observations.

4. Observations dealing with the CMB have been extensively performed. The Cosmic Background explorer (COBE) team [3] firstly discovered the anisotropy in the CMBR. With better angular resolution, the WMAP mission mapped the CMBR temperature anisotropy over the whole sky [4], and the Planck mission improved the WMAP data, and reduced the uncertainties due to dust contamination owing to its ten times better sensitivity and two times better angular resolution [5]. These observations have shown that the Universe was almost homogeneous with very small density perturbation

about 10^{-5}. These tiny variations in the density of matter leave an imprint in the CMBR in the form of temperature fluctuations of 0.0002K from point to point across the sky.

5. Using the observations of the CMB, one can assign initial conditions under which the first stars have formed. Such conditions are different from the contemporary star formation process, yet not as simpler as it was once assumed. Actually, the chemistry network is relatively simple due to the lack of heavy elements, and there is no feedback from the surrounding, since these stars are the first to ever form in the otherwise homogeneous and almost uniform Universe. However, several studies have elaborated the physics input of the problem by including radiative feedback [6, 7], dark matter annihilation [8], as well as the primordial streaming velocities [9]. In addition, the including the effect of the magnetic field makes the work more complex and challenging. This will be described later.

6. The formation, evolution and the death of Pop III stars enabled the transformation of the homogeneous inter galactic medium (IGM) consisting mainly of neutral hydrogen and helium gas floating in a sea of CMBR, into the IGM with rich structure we observe today (see [10]). Since there are no direct observations of these first stars, one can only rely on a theoretical approach in order to characterize their properties.

7. In the formation of the first stars, the role of dark matter is an essential ingredient besides gravity. The particles of dark matter collapse in the considered minihalos and dragged baryons along into their gravitational potential well until they reached a number density of $10^4\,\mathrm{cm}^{-3}$. later on, the baryons decoupled from dark matter and collapsed under their own self-gravity to form stars (see reviews by [11, 12] and references therein). The formation, evolution and final stages of Pop III stars depend crucially on their achieved mass, stellar rotation, and the effect of magnetic fields [13], where the most crucial parameter is the stellar mass since it determines the star's luminosity lifetime, end stage and chemical footprint.

8. As argued in the work by [14], very massive zero-metal stars of masses more than $120M_\odot$ are unstable due to nuclear-powered radial pulsation on the main sequence, nevertheless, they do not suffer appreciable mass loss because the growth time scale of the pulsation instability is much longer than for the metal-rich counterparts. A still open issue is the mass distribution, or initial mass function (IMF) of the Pop III stars.

The initial mass of the Pop III stars is a determining factor of their evolution till the end stage. In particular, as mentioned above if mass loss will not reduce the initial mass effectively, then the end stages is characterized by a peculiar supernova triggered by electron positron pair creation (briefly:

PCSN) powered by explosive oxygen burning. The calculations by [15] and [16] suggest a mass range about $M_* = 120 - 260 \ M_\odot$ for the PCSN, otherwise black hole formation would be the end stage. A successful PCSN leads to total disruption of the star and leads to first early heavy element enrichment in the universe only up to the iron group element as a result of explosive oxygen burning. If the Pop III stars would have been formed with low masses, they would have been observable presently (see [17]). However, that has never been the case.

9. Interesting to emphasize that the formation of the first stars may have been the sites where the seed cosmic magnetic field has been augmented to dynamically significant level by the process called "Biermann battery" and trough turbulent dynamo [18].

Summing up the introduction, the scope of this work represents a tight connection of star formation with cosmology. Therefore, it plays a unique role in the evolution of the universe. Not only fundamental interesting physics is involved in this subject, but it needs sophisticated and challenging numerical simulation.

In this present work project, we have used realisitic cosmological initial conditions calibrated by observation to follow the non-equilibrium evolution of the primordial gas. We included the magnetic field in the simulation in different ways: starting from an initial tiny seed field to study its amplification, or introducing the fully developed field at a later stage, in accordance with analytical models of the expected equipartition process.

The main emphasis in the present work is to investigate the effect and impact of the magnetic field on the process of the formation of the Pop III stars. The situation concerning the cosmic magnetic field has changed essentially after realizing that small-scale turbulent dynamo can be efficiently amplifying small primordial seed field to saturation value, especially that this process would be acting on a time scale shorter than the dynamical free-fall time. Magnetic energy density at saturation seems to reach 0.1% to 10% of the kinetic energy density. Magnetic fields with that strength can affect the evolution of the protostellar accretion discs. They remove angular momentum from the star-forming gas, drives jets and reduce the fragmentation in a disc [19, 20]. As expectation, Pop III clusters with few members with higher masses than predicted by hydrodynamic simulations.

Chapter 2

Review of literature works

The process of the formation of the first stars in the Universe has received remarkable effort during the last two decades. Different numerical approaches have been utilized, which led to a standard picture. In this chapter, we review these numerical approaches, the standard picture of the formation process as well as the frontiers of this topic.

In this chapter, these numerical approaches are reviewed to highlight the importance of the formation process of the first stars. Chapter 2 focuses on the formation of the Pop III stars on the basis of a hydrodynamic approach (Sec.. 2.1), while Sec. 2.2 concerns the formation process including a magnetic field.

2.1 Observational efforts and innovation

A new era begun after the operation of the James Webb Space Telescope (JWST) in exploring the early universe. In particular, better information concerning first stars may be obtained. The capabilities of the JWST are summarized in [21], as well as in the monograph by [22]. In addition to the space telescope, there are ground-based telescopes under construction that will allow astronomers to look further back in the history of our Universe, and provide information on the physics of the early Universe. The Giant Magellan Telescope (GMT)[1] will be ten times more powerful than the Hubble Space Telescope and have four times the imaging resolution of the JWST. The Thirty Meter Telescope (TMT)[2], will explore the period of formation of the first stars and galaxies. The European Extremely Large Telescope (E-ELT)[3] will be the largest ground-based telescope and will enable detailed studies of the first galaxies in the Universe, supermassive black holes. Complementary to them are ongoing and future meter-wavelength radio arrays, designed to detect the redshifted 21-cm radiation from the neutral

---

[1]https://giantmagellan.org/
[2]https://www.tmt.org/
[3]https://elt.eso.org/

hydrogen in the early Universe (see the review by [23]). A further intriguing window into the epoch of the first stars is provided by high-redshift gamma-ray bursts (GRBs). These are extremely bright, relativistic explosions, triggered when a rapidly rotating massive star is collapsing into a black hole.

According to the work by [24], it seems that the first stars are promising GRB progenitors. An alternative channel is related to the so called "Near field Cosmology" dealing with sources of redshifts after the dark age epoch (see [25]). By scrutinizing their chemical abundance patterns, the extremely metal-poor halo stars are useful objects to derive constraints on the properties of the first supernovae, which may have the Pop III star as their progenitors (for reviews, see [26, 27]).

Another class of relic objects is made up of the newly discovered extremely faint dwarf galaxies in the Local Group. These ultra-faint dwarf (UFD) galaxies consist of only a few hundred stars, and reside in very low-mass dark matter halos. Their chemical and structural history is therefore much simpler than what is encountered in massive, mature galaxies, and it should be much more straightforward to make the connection with the primordial building blocks [28].

Pop III stars are still not observed despite of great effort, so that they are still in the domain of theoretical modeling. What has been observed are Pop II stars with increasingly low metallicity, such as the newest ultra-metal poor halo star SMSS J160540.18-144323.1 where iron has been detected at a level $[Fe/H] =$ - 6.2 ± 0.2 according to [29]. This star has been discovered with the SkyMapper telescope, Australia. The star SMSS J031300.36-670839.3, however, the iron lines were not detected which places an upper limit on the iron abundance of the star, $[Fe/H] < -7.1$, at a 3σ confidence level [30].

Indeed, a number of extremely metal poor stars (EMPs) have been discovered in the Milky Way and in nearby dwarf galaxies [31–33], including the close-to-primordial star SDSS J1029151+172927 with $Z < 10^{-5} Z_{\odot}$ at the heart of the Lion ([34, 35]) and the most metal-poor star known J0023+0307 [36]. Moreover, an ultra metal-poor (UMP) binary star system 2MASS JJ1808-5104 was observed [37, 38]. The secondary star has a mass $M_2 = 0.14 M_{\odot}$, implying the possibility of the survival of solar-mass fragments around massive Pop III stars.

The observation of the elemental abundance patterns in extremely metal-poor stars (EMPs) is called stellar archaeology [26, 39]. It represents an alternative to direct observations, since EMPs likely formed from a gas enriched by individual supernova (SN) types i.e. the death of Pop III stars [40,41]. Hence, their chemical signature provides evidence and more insight on the earlier generation of Pop III stars [42].

2.2 The Canonical Cosmological Model

The adopted ΛCDM model takes into account the effect of cold dark energy as indicated by the cosmological constant Λ, the ordinary matter and the dispersion free cold dark matter (briefly: CDM). We adopt this model as a framework for the formation of the first stars in the sense that the first stars are thought to form in dark matter minihalos of about $\sim 10^6 M_\odot$ at redshift $z \sim 20 - 30$. In the following, the underlying formation scenario is introduced.

2.2.1 Basic physics

The Observations of the CMB [3, 4, 43] have shown that the Universe was initially almost homogeneous with tiny density perturbation of order 10^{-5}. The dynamically dominant dark matter pulls the baryonic gas into the so-called 'dark matter minihalos', such that the gas gets decoupled from the Hubble expansion and collapses, creating a state of "virial equilibrium" described by an equality between kinetic and gravitational potential energy:

$$\frac{GM_{\mathrm{halo}}}{R_{\mathrm{vir}}} \approx v_{\mathrm{vir}}^2 \, , \tag{2.1}$$

where M_{halo} is the total halo mass, and R_{vir}, v_{vir} are the virial radius and velocity, respectively. One can also define the halo density when the collapse has ended from the theory of gravitational instability [44]:

$$\rho_{\mathrm{vir}} = 200\rho_{\mathrm{b}} \, , \tag{2.2}$$

where $\rho_b = 2.5 \times 10^{-30} \left(1 + z\right)^3$ g cm^{-3} is the background density. The virial radius of a minihalo also depends on the redshift given by:

$$R_{\mathrm{vir}} \approx 200\mathrm{pc} \left(\frac{M_{\mathrm{halo}}}{10^6 M_\odot}\right)^{1/3} \left(\frac{z+1}{10}\right)^{-1} \left(\frac{\Delta_{\mathrm{c}}}{200}\right)^{-1/3} \, , \tag{2.3}$$

where $\Delta_{\mathrm{c}} = \rho_{\mathrm{vir}}/\rho_{\mathrm{b}}$ is the overdensity after virialization is complete [45]. The virial temperature corresponding to the virial velocity is found from $k_{\mathrm{B}} T_{\mathrm{vir}} \sim m_{\mathrm{H}} v_{\mathrm{vir}}^2$. It is then given by:

$$T_{\mathrm{vir}} \approx 2 \times 10^3 \mathrm{K} \left(\frac{M_{\mathrm{halo}}}{10^6 M_\odot}\right)^{2/3} \left(\frac{z+1}{20}\right) \, . \tag{2.4}$$

Barkana and Loeb [45] derived a lower limit on the mass of a gravitationally unstable body, from the theory of the growth of small density perturbations in an expanding Universe. From the interplay of gravity and thermal pressure, a critical length scale, termed Jeans length, is defined at a stage beyond which perturbations grow under their own self-gravity. On a scale smaller than the

Jeans length thermal pressure prevents the growth of the perturbation. The Jeans length is given in physical units by:

$$\lambda_{\rm J} = c_{\rm s} \left(\frac{\pi}{G\rho_0} \right)^{1/2} \ , \tag{2.5}$$

where $c_{\rm s}$ is the sound speed in the unperturbed intergalactic medium and ρ_0 is the cosmological background density. Jeans mass, the minimum mass of a gravitationally unstable perturbation, is the mass within a sphere of radius $\lambda_{\rm J}/2$, such as [45]:

$$M_{\rm J} = \frac{4\pi}{3} \rho_0 \left(\frac{\lambda_{\rm J}}{2} \right)^3 \ . \tag{2.6}$$

At high redshift, $M_{\rm J}$ can be approximated, using the instantaneous value of the sound speed at the relevant redshift, so that the jeans mass is given in this this case by [45]:

$$M_{\rm J} = 1.35 \times 10^5 \left(\frac{\Omega_{\rm m} h^2}{0.15} \right)^{-1/2} M_\odot \ , \tag{2.7}$$

where $\Omega_{\rm m}$ is the dimensionless parameter of cosmological matter density parameter, and h is the value of the Hubble constant in units of 100 km s^{-1} Mpc^{-1}.

For gravitational collapse to lead to star formation, the unstable gas must be able to sufficiently cool, as well. In the work by [46], various cooling channels of primordial gas were considered to derive the critical mass for cooling:

$$M_{\rm cool} = 6 \times 10^5 M_\odot h^{-1} \Omega_m^{-1/2} \left(\frac{\mu}{1.22} \right)^{3/2} \left(\frac{z+1}{10} \right)^{3/2} \ , \tag{2.8}$$

where μ is the mean molecular weight of the primordial gas. The mass of the halos that were able to radiatively cool depends strongly on the redshift. At $z \sim 100$, $M_{\rm b} = 5 \times 10^3 M_\odot$ and increases to $\sim 10^6 M_\odot$ at $z \sim 15$, due to effective molecular cooling. This cooling is essential for the formation of stars inside these minihalos. Only 10^{-3} of all baryons may have formed luminous objects by $z = 30$, which could be sufficient to reheat the Universe .

At high redshift, the baryonic gas is gravitationally bound to dark matter minihalos, as was established analytically by [47]. Soon after this pioneering paper by Tegmark [47], several numerical AMR simulations [48,49] with increasingly high resolution verified his analysis. The baryonic gas collapses into the dark matter gravitational well, and cools via H$_2$ cooling, such as at density of $\sim 10^4$ cm^{-3}, the temperature is ~ 200K and the mass of the gravitationally unstable core is $\sim 1000 M_\odot$. This core collapses rapidly in an inside-out fashion when the molecular hydrogen fraction exceeds $\sim 5 \times 10^{-4}$, to eventually produce a fully molecular hydrogen core of less than a solar mass that accretes at a rate of $\sim 10^{-3} M_\odot$/yr. [50] independently verified these results using smoothed particle hydrodynamics (SPH) simulations. Hence, a consensus was established that the

final star will be massive, as it would accrete $\sim 100 M_\odot$ in a Kevin-Helmholtz time of 10^5 yr, which is the time needed for a star to reach the main-sequence [48].

The initial stellar mass is a crucial parameter in determining their overall impact on the early Universe [16,17]. The evolutionary calculation of non-rotating zero -metallicity stars and of initial masses in the mass range $15 < M_*/M_\odot < 40$ end their evolution as core-collapse supernovae. The end stage of stars with initial masses in the range $140 < M_*/M_\odot < 260$ is a total explosion by explosive oxygen burning initiated by pair creation instability which leads to pair creation supernovae (PISNe). Larger masses end up as block holes in the mass range $40 < M_*/M_\odot < 140$ or $M_*/M_\odot > 260$. But the initial mass function (IMF) remains rather uncertain and controversial.

Early simulations suggested the formation of stars with masses above $100 M_\odot$ [48,50–52], but more recent work argued that the fragmentation of the accretion disks around Pop III protostars was not accurately resolved in earlier studies due to limited numerical resolution [53–55]. The fragmentation results in multiple systems with masses between 10 and $100 M_\odot$. Similarly, [56] argued that the central core of $50 M_\odot$ could fragment into a binary system of 10and6$M_\odot$. In extreme cases, this range might even extend down to 0.1 $M_\odot$ [8]. However, [57] constrains the lower mass IMF limit to 0.65 $M_\odot$ with a confidence of 95 per cent. The question remains to ask where all these stars are. Recent three-dimensional, gravito-radiation-hydrodynamics simulations [7,58–60] examine in detail how massive the first stars can grow during the accretion phase. In particular, [7] found that the masses are typically of the order of $100 M_\odot$. While, [61] found a mass distribution with two peaks at ~ 25 and $250 M_\odot$. [62] followed the collapse for $\sim 10^5$yr and found that all secondary fragments merged into the central star, hence forming only one star in each of their five minihalos. In contrast, [63] found that Pop III multiple systems are common, where most minihalos formed a median of four Pop III stars each. Therefore, the multiplicity and final mass of the first stars is still a serious matter of debate.

Is it possible to estimate the lower limit of Pop III stars? According to the work by [64], the initial hydrostatic core has a mass, $M_{\mathrm{core}} \sim 10^{-2} M_\odot$, at the beginning of the main accretion phase, given by the classical theory of opacity-limited fragmentation. This lower-limit mass is very similar to present-day proto-stellar seeds [11], because core masses only weakly depend on environmental variables, such as gas temperature and metallicity [64,65], such as $M_{\mathrm{F}} \propto f^{-1/2}T^{1/4}$, with $f = f(Z) \lesssim 1$ is an efficiency factor depending only weakly on metallicity, Z, and other factors, such as collapse geometry and clumpiness of the medium [11]. The protostellar core continues to accrete mass from the ambient material [66,67]. Its final mass would then depend on the fraction of the cloud's mass that can form be incorporated into the star. For Pop I star formation, spherical accretion above a mass of $\sim 15 M_\odot$ is difficult due to the radiation force on dust grains, yet non-spherical accretion may enhance the maximum stellar mass [51].

The mass accretion rate can be estimated by assuming that gas of mass $M =$

M_J collapses on its free-fall timescale [68]:

$$\dot{M} \approx \frac{M_J}{t_{\rm ff}} \approx \frac{c_s^3}{G} \propto T^{3/2} \; . \tag{2.9}$$

The temperature is substantially higher in primordial gas ($1000 - 1500$ K over a wide density range [66]) than in contemporary star forming clouds (~ 10 K). The minimum possible temperatures in primordial gas due to H_2 cooling is ~ 200 K, and including more efficient cooling like HD molecules, the temperature could reach the CMB floor $T_{\rm CMB} \approx 11(1+z)/4$ K, which is higher than 10 K for $z \gtrsim 3$. Thus, the accretion rates in Pop III stars is larger than in Pop I stars, by at least two orders of magnitude. This would then lead to the formation of very massive stars, reaching more than $100 M_\odot$ [11,69]. Moreover, another argument for forming a massive central star is that, even when fragmentation occured, the fragments are dragged to the center through viscous forces, where they merge back into the central core [70]. Therefore, the question remains whether the fragments get ejected from the cloud center through N-body dynamics, representing candidates for Pop III survivor or they merge back into the central core and form a massive short-lived star.

2.2.2 Basic processes

The primordial gas mainly of Hydrogen and Helium, in minihalos of Dark Matter decoupled from the expansion of the Universe and formed the first stars. The baryonic gas experiences different chemical and thermal processes leading to an initial collapse and a formation of an accretion disc.

Contrary to earlier belief, the chemothermal evolution of the primordial gas clouds is rather complex, being coupled with the dynamical evolution of dark matter halos [71,72]. Simple analytic models also fail in predicting the evolution of primordial gas in CDM halos [73]. It is also important to include the effect of the opacity of the cloud core. Otherwise, the radiative cooling rate can be overestimated at the cloud center, leading to uncertainties in fragmentation and mass accretion.

In this section, we discuss the evolution of the gas from the mostly atomic state until the formation of the hydrostatic core and accretion disc.

Below $n = 1\,{\rm cm}^{-3}$, the baryonic gas is bound to DM and its collapse heats up the gas due to compressional heating up to maximum temperatures of $T \sim 1000$ K, close to the virial temperature of the host minihalo [54,69,74,75]. Meanwhile H_2 molecules are forming via the H^- channel [76] until reaching an asymptotic fraction value of $f_{H_2} = 10^{-3}$ [48,50,71]. This small fraction of molecule Hydrogen is able to cool the gas through H_2 rovibrational transitions to temperatures of about ~ 200 K at density $10^4\,{\rm cm}^{-3}$, the point at which the gas decouples from the DM and becomes self-gravitating [50]. This corresponds to the 'loitering' state, when the cooling rate dependence on density changes from

$\Lambda_{\rm cool} \propto n^2$ to $\Lambda_{\rm cool} \propto n$, making the H_2 cooling less efficient toward higher densities [50]. This loitering point is reached, if H_2 is the only low-temperature coolant included. The Hydrogen Deuteride (HD) may also cool the gas to the CMB floor temperature [50], most likely in the lowest mass minihalos [77].

At $n = 10^8\,{\rm cm}^{-3}$, the three-body reactions leads to enhanced formation of H_2 molecules [66], converting the gas into fully molecular form [66] by $n \sim 10^{12}\,{\rm cm}^{-3}$. The chemothermal instability associated with this transition to fully molecular gas may in turn be able to induce fragmentation already during the initial collapse, on scales of $\sim$10 AU in $\sim$1/3 of minihalos [78]. The rates of the three-body reactions are still uncertain, yet they show reasonable agreement at high temperatures ($T > 5000$ K), and show an uncertainty by an order-of-magnitude at low temperatures relevant to Pop III star formation (20 K $< T <$ 200 K) [19,79]. This uncertainty will inevitably induce huge uncertainties in the high-density thermal evolution, morphology, radial velocity and accretion rate, as shown by [19].

At densities above $n > 10^{12}\,{\rm cm}^{-3}$, the ro-vibrational lines of H_2 become increasingly optically thick, until becoming completely optically thick throughout, at densities $n > 10^{14}\,{\rm cm}^{-3}$ [67,80]. An escape probability method, combined with the Sobolev approximation has been used in simulations to be able to follow the collapse in this phase [52,70,81–83]. The escape probability used is given by:

$$\beta_{\rm esc} = \frac{1 - \exp(-\tau)}{\tau} \; , \qquad (2.10)$$

where the line optical depth is $\tau = k_{\rm lu} L_{\rm char}$.
Here, $\tau = k_{\rm lu}$ is the absorption coefficient in the given line, and $L_{\rm char}$ is a length characteristic of the line-formation region.

H_2 molecules have no electric dipole, but the collision between two H_2 molecules results in the H_2-H_2 "supermolecule", possessing an induced electric dipole moment [84, 85]. Hence, this non-zero electric dipole leads to a high probability of emitting or absorbing a photon. These processes are called collision-induced emission (CIE), and its reverse absorption process (CIA), respectively. The interacting pairs H_2–He, H_2–H and H-He perturb each other and emit (or absorb) a photon through a dipole transition [85]. The CIE cooling become effective for densities $n > 10^{14}\,{\rm cm}^{-3}$.

At the highest densities ($n > 10^{16}\,{\rm cm}^{-3}$), the gas cools down via the collisional dissociation of H_2 that removes the binding energy of 4.48 eV per molecule from the otherwise already optically-thick gas. The net thermal effect is a near-isothermal collapse at $T \sim 1000$ K [54]. Beyond this point, following the non-equilibrium chemistry becomes computationally expensive, since timesteps drop abruptly, reflecting the increasingly short reaction timescales at high density [50]. When this happens, it's common to switch to an equilibrium solver, as done by [70], since the evolution proceeds roughly isothermally due to the approximate balance between compressional and H_2 formation heating and enhanced H_2

cooling. However, with increasing density, H_2 line opacity, CIE and H_2 dissociation dominate [11].

In realistic three-dimensional simulations, the radial density profile, $\rho \propto r^{-n_\rho}$, with an exponent, $n_\rho = 2/(2-\gamma)$, determined by the equation of state, $P \propto \rho\gamma$. This solution is spherically symmetric Larson-Penston (LP) type similarity solutions [86, 87]. In the work by [67] for Pop III, based on one-dimensional radiation-hydrodynamics simulation, , it was found that $n_\rho \approx 2.2$, corresponding to an adiabatic exponent of $\gamma \approx 1.1$, indicating a near-isothermal collapse [11]. More recently, using three-dimensional simulations, [70, 88, 89] found an exponent $n_\rho = 2.22$, 2.3 and 2.16.

A hydrostatic (protostellar) core is formed when the primordial gas becomes opaque to its cooling radiation as mentioned above [64], at number densities of $n \gtrsim 10^{20}\,\mathrm{cm}^{-3}$. Except that the protostar is not defined by its number density. Its extent may be defined by its photosphere, where the optical depth is $\tau \sim 1$, since, as previously discussed, the core becomes optically thick. A second definition is also possible by determining its 'hydrostatic radius', where the radial (infall) velocity is near zero, indicating the state of hydrostatic equilibrium [70]. It is emphasized that the hydrostatic radius is smaller than the photospheric one, based on the standard theory of early protostellar structure [90]. The structure of a primordial protostar constitutes a hydrostatic core in the center, influenced by accretion shock. The infalling material diffuses upstream through the optically thick radiative precursor. Then at the photosphere ($R_\mathrm{p} = 1.4 R_\mathrm{core}$), the photons break free of the infalling gas and leave the cloud through the optically thin outer envelope [90].

2.3 Extension of the Adopted Cosmological Model

A variety of physical processes can affect and may substantially alter the picture outlined above, such as cosmic rays, streaming velocities, dark matter properties and magnetic fields. In this work, we we focus on the effects of the magnetic field on the formation process of the Pop III stars.

Several reasons make the generation and amplification of cosmic magnetic fields of great interest. Understanding the generation and amplification of cosmic fields is essential to elucidate the evolution of the Universe. Moreover, theoretical prediction on the generation of magnetic fields helps in determining their local structure by observational techniques, that usually average the fields over large distances.

In addition, in order to address the astrophysical and cosmological problems such as the formation of the first stars and first galaxies, it is important to know the direction and strength of magnetic field, the magnetization of the media and the 3D distribution of these characteristics in various media phases.

2.3.1 Observations of IGM magnetic field

It is well established that microgauss fields exist in present-day galaxies of all types as well as in galaxy clusters [91–93]. Magnetic fields have been observed in stars [94] and black holes [95], on galaxy scales such as in our own Milky Way [96], in galaxy groups and clusters [97], and finally in the intergalactic medium [91,98]. More significant to our work is, however, magnetic field strengths in intermediate and high redshifts.

High resolution rotation measures (RMs) of very far quasars have allowed to probe magnetic fields in the distant past. The most significant measurements are due to Kronberg [91]. RMs of the radio emission of the quasar 3C191, at $z = 1.945$, presumably due a magnetized shell of gas at the same redshift, are consistent with a field strength in the range $0.4 - 4\,\mu$G. The magnetic field of a relatively young spiral galaxy at $z = 0.395$ was determined by RMs of the radio emission of the quasar PKS 1229-021 lying behind the galaxy at z = 1.038 [99]. The magnetic field amplitude was firmly estimated to be in the range $1 - 4\,\mu$G. Estimates suggest that the fields in galaxies at redshift $z \sim 1.3$ are comparable to those in present-day galaxies [92].

The most common element in the ISM is the neutral Hydrogen. The hyperfine structure of hydrogen corresponds corresponds to the 21-cm line emission of neutral Hydrogen. The presence of a magnetic field produces a well known splitting of the spectral lines:

$$\Delta\nu_{\mathrm{Z}} = \frac{eB_{||}}{2\pi m_{\mathrm{e}}} \ .$$

(2.11)

Hence, the magnetic field intensity can be deduced from the estimate of the spectral lines splitting. The direct observation by the Zeeman splitting of spectral lines can be useful in our galaxy. For more distant objects, possible observations are those dealing with the strength and spatial distribution of the magnetic field [98]. The intensity and the polarization of synchrotron emission from free relativistic electrons can be used as well as the Faraday rotation measurements (RMs) of polarized electromagnetic radiation passing through an ionized medium [91]. Evidence of magnetic fields of a maximum of $1\,\mathrm{cm}^{-3}$ in clouds with redshift larger than 1.0 are obtained.

In contrast to the magnetic field observed in galaxies, magnetic fields along filaments and voids of the cosmic web still reflect the seed field intensity. Tiny but significant magnetic fields appear to exist in cosmic voids, as suggested by γ-ray experiments [100–102], filling more than 60% of the volume [102]. An observational lower limit of the order $10^{-15}\,$G has been derived on this field strength based on FERMI observations of TeV blazars [100]. TeV γ-ray photons pass through voids from distant extragalactic blazars with known flux. When these photons interact with the extragalactic background light, they create electron/positron pairs traveling in the same direction as the original photon and produce

an observable electromagnetic cascade emission. However, the expected flux is orders of magnitudes higher than the current upper limit obtained with FERMI, which implies that magnetic fields deflected charged particles from the line of sight [103].

Several techniques have been used to detect the extremely weak unamplified extragalactic magnetic fields (EGMFs). Measurements of the Faraday rotation in the polarized radio emission from distant quasars [91, 104, 105] and/or distortions of the spectrum and polarization properties in the cosmic microwave background (CMB) radiation [106–109] imply upper limits on EGMF strengths at the level of $\sim 10^{-9}$ G. Numerical modeling of magnetic field formation in galaxy clusters implies a theoretical upper bound of the order of $\sim 10^{-12}$ G on EGMF strength [110, 111].

A primordial magnetic field (PMF) affects the temperature fluctuations of the CMB as well as their polarization, since it is an additional relativistic species in the cosmological plasma before recombination [112, 113]. It is possible to constrain the PMF amplitude at the nG on the 1 Mpc scale, from both the gravitational effects on cosmological perturbations [109] and non-Gaussian behavior [108]. An upper limit of $B \lesssim 10^{-9}$ G is placed by studying the CMB B-mode perturbations [108, 114] and lower limits of $B \gtrsim 10^{-17}$ G are available from γ-ray particle cascades [100].

2.3.2 Origin and amplification of magnetic fields

Regardless of their recognized presence and importance in all the environments discussed above, many details regarding their evolution and particularly their origin remain unknown. Several theories have been presented to explain the observed magnetic field in the Universe. The observed magnetic fields is thought to be the result of an amplification of much weaker seed fields of uncertain origin.

Theoretical models predict several mechanisms for its generation (reviews by [115, 116]). Cosmological models suggest that the seed fields are produced in the early Universe. Astrophysical models suggest that they may have been generated by motions of the plasma in (proto)galaxies [91, 98].

One possibility is, therefore, that the cosmic magnetic field is primordial, e.g. the magnetic field was created with the birth of the Universe. In this case, weak magnetic fields would be observed in the darkest spot of our Universe and an unambiguous magnetic signature in the CMB should be observed. According to Jedamzik [117], a pre-recombination PMF of strength ~ 0.1 nG [118, 119] could explain the origin of galactic, cluster, and extragalactic magnetic fields. In addition, primordial magnetic fields (PMFs) may induce additional baryon inhomogeneities in the pre-recombination era (e.g. analytically derived in [118], and numerically reproduced in [119]), which enhances the recombination rate and leads to higher value of the Hubble constant. This mechanism results in explaining why the Universe is expanding significantly faster than expected, e.g.

the Hubble tension [117].

PMFs are expected to have random orientations and strengths [120]. Since the diffusion time of a magnetic field in galaxy clusters is much longer than the age of the Universe, such a magnetic field is "frozen-in" to the ionized fluids [121]. The energy density of the baryon fluid scales as $\rho_\mathrm{b} \propto a^{-3}$ while the magnetic energy density scales as $\rho_\mathrm{B} \propto a^{-4}$. Therefore, one can relate the strength of the magnetic field energy density to the energy density of the cosmic baryon fluid $B^3 \propto \rho_\mathrm{b}^2$. If clusters of galaxies collapse nearly isotropically relative to the background space, an observed magnetic field of B $\sim 1\mu$G in galaxy clusters now corresponds to a PMF of order $\sim 1.0\,$nG at the epoch of photon last scattering near z ~ 1100.

Some theories involve primordial vorticity during the radiation era of the early Universe [122]. Other models invoke phase transitions that occur during cosmic inflation [92, 98, 123]. The work by [124] showed that a magnetic field could be generated by quantum perturbations. For PMFs generated, at the cosmological quark-hadron [125, 126] or electroweak [127] phase transitions, bubbles of a new lower temperature phase collide, leading to the break of the baryon symmetry which generates a magnetic field [125]. Fields generated by the quark-hadron transition have been estimated to be $\sim 10^{-7}\,$nG in [125], and those generated during the electroweak transition have been estimated to be $\sim 10^{-14}-10^{-18}\,$nG [127]. Eddies before the recombination epoch could generate a PMF, as seen in [128]. But even without turbulent eddies, the known CMB temperature fluctuations imply the generation of at least some magnetic primordial field. The difference in the electron scattering of photons and protons induce electric currents as they fall in and out of gravitational potentials. These electric fields can generate a magnetic field of about $10^{-9}\,$nG at 1 Mpc [128].

Alternatively, cosmic magnetic fields may be created by astrophysical mechanisms: During the inflationary epoch or later, via the so-called "Biermann battery" (e.g. [129, 130]), or via the Weibel instability [131, 132] or thermal plasma fluctuations [133]. The magnetic induction equation takes the form:

$$\frac{\partial \boldsymbol{B}}{\partial t} = \nabla \times (\boldsymbol{v} \times \boldsymbol{B}) + \frac{c}{n_\mathrm{e}^2 e} \boldsymbol{\nabla} p_\mathrm{e} \times \boldsymbol{\nabla} n_\mathrm{e} \ , \qquad (2.12)$$

where $\boldsymbol{B}$ is the magnetic field, $\boldsymbol{v}$ is the velocity, n_e the electron density, p_e the electron pressure and e is the electron charge.

The source term of the induction equation is caused by the misalignment of the electron density gradient with the gradient of electron pressure. This can happen in a partially ionized gas when the temperature gradient does not align with the pressure gradient, which leads to a generation of magnetic field even when the initial magnetic field is zero. Theoretical expectations based on the Biermann battery term [129] are consistent with the observational constraints discussed above. In a cosmological MHD simulation, the generation of magnetic fields was followed based on the Biermann battery effect [130], finding IGM magnetic fields of $10^{-15}\,$G at $z \sim 10$, which may naturally explain the observed lower limits.

Additional seed fields may be created by the Weibel instability in shocks [131]. Even stronger magnetic fields may have been created in the Universe before recombination [98, 134].

In each case, the inferred field strengths are very small to be dynamically important. But such seed fields could be quickly amplified to equipartition with the kinetic energy in protogalactic clouds due to small-scale dynamo action or turbulence [135–137]. The small-scale turbulent dynamo, which is very efficient in amplifying even extremely small primordial seed fields to the saturation level. This process is very fast and acts on timescales much shorter than the dynamical free-fall time. An analytic treatment is possible in terms of the Kazantsev model [136, 138–140]. Once backreactions become important, the growth rate slows down, and saturation is reached within a few large-scale eddy turnover times [141]. Depending on the properties of the turbulent flow, the magnetic energy density at saturation is thought to lie between 0.1% and a few 10% of the kinetic energy density [142–144]

The prediction of linear dynamo, by Kronberg [91], imply an equipartition between turbulent motion and magnetic energies in galaxies. Several methods allowed the determination of the interstellar magnetic field in the Milky Way. The average field strength is $3 - 4\,\mu$G corresponding to an approximate energy equipartition between the magnetic field, the cosmic rays confined in the Galaxy, and the small-scale turbulent motion [91, 98]:

$$\rho_{\mathrm{m}} = \frac{B^2}{8\pi} \approx \rho_{\mathrm{t}} \approx \rho_{\mathrm{CR}} \; . \tag{2.13}$$

The strength of the primordial field that could be amplified into the observed strength in the Milky Way $\sim \mu$G was estimated in [145]. First, the flux freezing during gravitational collapse amplifies the field by a factor $(\rho_{\mathrm{gal}}/\rho_{\mathrm{b}})^{2/3} \sim 10^5$, where $\rho_{\mathrm{gal}} \approx 10^{-24}\,\mathrm{g\,cm^{-3}}$ is the baryon density in the Milky way and $\rho_{\mathrm{b}} \sim 10^{-31}\,\mathrm{g\,cm^{-3}}$ is the average cosmological baryon density. Therefore $\sim 10^{-11}\,\mathrm{G}$ cosmological magnetic fields can generate galactic field strength $\sim \mu\,\mathrm{G}$ simply by gravitational compression. In addition to gravitational compression, a maximally efficient dynamo would amplify the field strength by an e-fold with each full rotation of the galaxy. The seed field B_{seed} required to explain the Milky Way magnetic field would then be $\sim e^{-N_{\mathrm{rev}}} (\rho_{\mathrm{gal}}/\rho_{\mathrm{b}})^{-2/3} 10^{-6}\,\mathrm{G}$, where N_{rev} is the number of complete revolutions of the Milky way, estimated to be 40. This seed field $\sim 10^{-29}\,\mathrm{G}$ is possible from the Biermann battery mechanism [135, 146].

2.3.3 Numerical treatment of the magnetic field

The effect of magnetic field on the formation and evolution of contemporary stars has been extensively investigated in numerical and theoretical studies (e.g. reviews by [147–150]). This led to a better yet incomplete understanding of the star formation process. Magnetized turbulence interacts with gravity to create

structures like filaments, clumps and clusters. Magnetic fields reduce the number of objects that form at all scales by a factor of a few only, contrary to the older belief that magnetic field drastically affects the star formation rate. With the magnetic field, the masses of the stars are also a few times larger than without including it, because the magnetic field tends to reduce fragmentation. Another effect of the magnetic fields is to alter the shape of the clouds which get flattened along the magnetic field, leading to a filamentary structure rather than a symmetric spherical cloud. Additionally, the magnetic braking that reduces the size of protoplanetary disks.

Due to the lack of observations of the early Universe, the magnetic field, at redshifts relevant to the current problem, hasn't been well constrained [116]. Hence, the numerical investigations are the main tool to investigate and predict the effect of the magnetic fields on the formation of the first stars.

Early studies of the formation of the Pop III star formation ignored the magnetic fields, because it was assumed that magnetic fields simply did not exist under these pristine conditions, or an existing seed field would not be dynamically important [46]. However, many investigations have included a magnetic field in their work (e.g. [18, 136, 151–158]), and more papers in the last few years (e.g. [89, 137, 144, 159–163]).

The first self-consistent simulation starting from cosmological initial conditions was done by [130] to study the possibility of generating dynamically important magnetic field *ab initio*. This was done by applying the so called "Biermann battery" [129], together with compressional amplification. In this way, a field of 10^{-9} G was achieved at $n = 10^{10}$ cm^{-3} in the center of the Pop III star forming cosmological halo in which the pop III star was formed. In contrast, [164] and [18] showed that substantially higher peak magnetic field strengths were generated when higher resolution was used. Therefore, deducing, that the amplification growth rate is resolution-dependent, so that a minimum resolution threshold is required to find any turbulent amplification. Similarly, the work by [152], argued that a comoving field of only 10^{-5} nG are amplified to values of ~ 1 nG at a density of 10^3 cm^{-3}. Such fields are required to drive protostellar outflows that can magnetize the IGM [165]. Comoving magnetic fields in excess of 0.1 nG increase significantly the thermal and magnetic Jeans mass in the IGM to $10^7 - 10^9 M_\odot$. Subsequent generations of stars may form from gas that has been enriched with metals, and presumably stronger magnetic fields due to stellar winds or supernova explosions. The authors in [153] have used a semi-analytical model to investigate the magnetic field amplification during the collapse, incorporating the effects of gravitational compression and small-scale dynamo amplification. Their results indicate that the magnetic field seems to be substantially amplified before the formation of a disk. The strength of the field at saturation in the first star-forming halo was of the order $\sim 10^{-7} n^{1/2}$ G. This was later confirmed theoretically by [136] using the "Kazantsev" theory, which describes the small-scale dynamo. The learn effect of these investigations is that

small-scale fields generated by the "Biermann battery" mechanism, are amplified rapidly to become dynamically important locally. The authors in [166] started with a field of strength $1\mu G$ corresponding to a magnetic to kinetic energy ratio ($E_B/E_k \sim 10^{-4}$), which is well below equipartition. Due to gravitational compression and the small-scale dynamo, a saturation value $E_B/E_k = 0.2 - 0.3$ was obtained. The saturation of the small-scale dynamo is marked by a change in the slope of $B/\rho^{2/3}$. According to [18, 154, 167], to generate dynamically important fields in the central collapsing core, the Jeans length should be resolved by at least 32 cells .

The investigation by [156] has shown that the effect of the field can be neglected below a critical value $B_{crit} = 10^{-13}(n_H/1\,cm^{-3})^{-2/3}\,G$ was found in . For magnetic fields below this critical value, fragmentation occurs frequently with the most massive protostar remains near the cloud centre, while some of the less massive protostars are ejected. For strengths above $10B_{crit}$, angular momentum transfer is effective through magnetic braking and protostellar jets, promoting the formation of a single massive star without forming a disc. In the investigation by [163], the finding was that magnetic field does not affect the temperature evolution of the central core, yet slows down the cloud contraction only in the directions perpendicular to the field lines. In the work by [144] isolated, initially-turbulent primordial cores, each with different initial field strength were considered and the magnetic field was found to inhibit fragmentation and favors the formation of single stars of high masses. In a subsequent paper, [160], these authors found a strong dependence on the initial conditions.

Another approach used by [161] was based on cosmological initial conditions and used a primordial chemistry network (similar to the approach used in the present work). It was found that the magnetic field delayed the gravitational collapse by $\Delta z = 2.5$ in redshift. For higher magnetic field strength, the collapse is completely suppressed and the mini-halos continue to grow. Another more recent work by [89] starting also from cosmological initial conditions, to compare the results of a simulation without magnetic field with another one including magnetic field effects at redshift $z = 25$, with a strength a little above the value predicted from the Biermann battery. The result was that the introduced field was amplified to a value close to half the equipartition value at number density $n = 10^8\,cm^{-3}$. The main effect of the magnetic field was to suppress fragmentation. These calculations suggest protostars of masses ~ 1 to $30\ M_\odot$ in the hydrodynamic case, whereas only a single protostar of $\sim 30M_\odot$ in case of the MHD calculation.

These results suggest that the masses of the first stars responsible for the early metal enrichment are predominantly $40M_\odot$. This implies that the higher-mass first stars were either less abundant, directly collapsed into a black hole without ejecting heavy elements, or a supernova explosion of a higher-mass first star inhibits the formation of the next generation of low-mass stars at [Fe/H] < -3 [168].

In the following we introduce the concept of equipartition, which is utilized in

the present work. Before the stage of equipartition, the field scales as $\rho^{2/3}$ [137] and gets amplified exponentially to the equipartition value given by:

$$B_{\text{eq}} = (4\pi\rho)^{1/2}v_{\text{t}} \ , \tag{2.14}$$

where v_{t} is the turbulent velocity. When the field reaches equipartition, it will increase as $\rho^{1/2}$ for constant turbulent velocity, and stops growing at the saturation value B_{sat} given by [137]:

$$B_{\text{sat}} = \phi_{\text{sat}}B_{\text{eq}} \ . \tag{2.15}$$

In case of subsonic solenoidal turbulence $\phi_{\text{sat}} = 0.65$ [169], $\phi_{\text{sat}} \approx 0.7$, according to [170, 171]. A value of $\phi_{\text{sat}} = 0.14$ is suggested by [170] in case of supersonic solenoidal turbulence. The magnetic Reynolds number in a typical cosmic minihalo is large, so flux freezing is a good approximation for the effects of compression. Subsequently, both the magnitude and the scale of the field grow as it reaches equipartition with larger and larger eddies. In the post-recombination Universe, ambipolar diffusion provides the dominant resistivity for fields $B > 10^{-13}n_{\text{H}}$G [137, 172].

Amplified fields affect the evolution of protostellar accretion disks: They remove angular momentum from the star-forming gas [151, 155, 156, 173], drive protostellar jets and outflows [165], and they reduce the level of fragmentation in the disk [19, 20], without affecting the thermal properties of the halos [155]. Magnetic fields generated by dynamo processes in the early Universe and ejected in outflows will also have implications for the formation of the second generation of stars and the first galaxies [166].

CHAPTER 3

METHODOLOGY

The investigation of the formation process of the first stars in the universe, the so-called Pop III stars, especially considering the effect of the cosmic magnetic field computational tools or simulations are required. Fortunately, open-source codes are available like ENZO, which helps to concentrate on the physical input.

In this chapter, we will describe the theoretical background (Sec. 3.1) and the numerical aspect of the numerical treatment (briefly: simulation), and the initial conditions are presented in Sec. 3.2. In Sec. 3.3, the chemical reaction network is presented. Sec. 3.4 describes the incorporation of the MHD effects.

3.1 Governing equations

The computational code `Enzo`[1] uses the Particle-Mesh N-body method to calculate collisionless particle dynamics. This method follows trajectories of a representative sample of individual particles and is much more efficient than a direct solution of the Boltzmann equation in most astrophysical situations. The particle trajectories are controlled by a simple set of coupled equations:

$$\frac{d\boldsymbol{x}_{\mathrm{p}}}{dt} = \boldsymbol{v}_{\mathrm{p}} \ , \tag{3.1}$$

$$\frac{d\boldsymbol{v}_{\mathrm{p}}}{dt} = -\boldsymbol{\nabla}\Phi \ , \tag{3.2}$$

$$\nabla^2\Phi = 4\pi G\tilde{\rho} \ , \tag{3.3}$$

where $\boldsymbol{x}_{\mathrm{p}}$ and $\boldsymbol{v}_{\mathrm{p}}$ are the particle position and velocity vectors, respectively, and the term on the right-hand side of the second equation is the gravitational force term and $\tilde{\rho}$ is the density of both the collisional fluid (baryon gas) and the collisionless fluid (particles).

---

[1] http://enzo-project.org

The governing equations for the baryons in a magnetic field are the mass conservation (Eq. (3.4)), the equation of motion (Eq. (3.5)), the gas energy equation (Eq. (3.6)), the induction equation for ideal MHD (Eq. (3.7)), the solenoidal constraint (Eq. (3.8)) and the Poisson equation of gravity (Eq. (3.3)):

$$\frac{\partial \rho}{\partial t} + \boldsymbol{\nabla} \cdot (\rho \boldsymbol{v}) = 0 \ , \tag{3.4}$$

$$\rho \frac{\partial \boldsymbol{v}}{\partial t} + \rho (\boldsymbol{v} \cdot \boldsymbol{\nabla}) \boldsymbol{v} = -\boldsymbol{\nabla} p - \frac{1}{4\pi} \boldsymbol{B} \times (\boldsymbol{\nabla} \times \boldsymbol{B}) - \rho \boldsymbol{\nabla} \Phi \ , \tag{3.5}$$

$$\frac{\partial e}{\partial t} + \boldsymbol{\nabla} \left[\left(e + p + \frac{|\boldsymbol{B}|^2}{8\pi} \right) \boldsymbol{v} - \frac{1}{4\pi} \boldsymbol{B} (\boldsymbol{v} \cdot \boldsymbol{B}) \right] = -\rho \boldsymbol{v} \cdot \boldsymbol{\nabla} \Phi - \Lambda_{\mathrm{cool}} \ , \tag{3.6}$$

$$\frac{\partial \boldsymbol{B}}{\partial t} = \boldsymbol{\nabla} \times (\boldsymbol{v} \times \boldsymbol{B}) \ , \tag{3.7}$$

$$\boldsymbol{\nabla} \cdot \boldsymbol{B} = 0 \ , \tag{3.8}$$

where ρ, p, $\boldsymbol{v}$ are density, pressure, velocity of the gas respectively. $\boldsymbol{B}$ is the magnetic field, Φ is the gravitational potential, e is the total gas energy per unit volume and Λ_{cool} is the net cooling rate per unit volume.

The hydrodynamic pressure p is given y the equation of state or a perfect gas:

$$p = (\gamma - 1) \left(e - \frac{\rho |\boldsymbol{v}|^2}{2} - \frac{|\boldsymbol{B}|^2}{2} \right) \ , \tag{3.9}$$

where γ is the adiabatic index, which depends on the chemical composition and gas temperature.
The adiabatic exponent is given by [67]:

$$\gamma_{\mathrm{ad}} = 1 + \sum_i \frac{n_{\mathrm{i}}}{\sum_i n_{\mathrm{i}} / (\gamma_{\mathrm{i}} - 1)} \ , \tag{3.10}$$

where the summation is over all chemical species and n_{i} is the number density of each species.
The adiabatic exponent for H_2 is given by:

$$\frac{1}{\gamma_{\mathrm{H_2}} - 1} = \frac{1}{2} \left[5 + 2x^2 \frac{e^x}{(e^x - 1)^2} \right] \ , \tag{3.11}$$

where $x = 6100\mathrm{K}/T$ and the second term in Eq. (3.11) describes the vibrational degrees of freedom. For species other than H_2, treated as monatomic gas, the term $1/(\gamma_{\mathrm{i}} - 1) = 3/2$.

If non ideal MHD effects are included, such as the ambipolar diffusion term, the induction equation (Eq. (3.7)) becomes:

$$\frac{\partial \boldsymbol{B}}{\partial t} - \boldsymbol{\nabla} \times (\boldsymbol{v} \times \boldsymbol{B}) = \boldsymbol{\nabla} \times \left\{ \left[\eta_{\mathrm{AD}} (\boldsymbol{\nabla} \times \boldsymbol{B}) \times \boldsymbol{B} \right] \times \boldsymbol{B} \right\}. \tag{3.12}$$

We emphasize that we do not include ambipolar diffusion in the present work. The cosmological MHD equations are modified as follows [174]:

$$\frac{\partial \rho}{\partial t} + \frac{1}{a} \boldsymbol{\nabla} \cdot (\rho \boldsymbol{v}) = 0 \ , \tag{3.13}$$

$$\frac{\partial \rho \boldsymbol{v}}{\partial t} + \frac{1}{a} \boldsymbol{\nabla} \cdot \left(\rho \boldsymbol{v} \boldsymbol{v} + \tilde{p} - \frac{\boldsymbol{B} \boldsymbol{B}}{a} \right) = -\frac{\dot{a}}{a} \rho \boldsymbol{v} - \frac{\rho}{a} \boldsymbol{\nabla} \Phi \ , \tag{3.14}$$

$$\frac{\partial E}{\partial t} + \frac{1}{a} \boldsymbol{\nabla} \cdot \left[(\tilde{p} + e) \boldsymbol{v} - \frac{1}{a} \boldsymbol{B} \left(\boldsymbol{B} \cdot \boldsymbol{v} \right) \right] = -\frac{\dot{a}}{a} \left(2E - \frac{|\boldsymbol{B}|^2}{2a} \right) - \frac{\rho}{a} \boldsymbol{v} \cdot \boldsymbol{\nabla} \Phi \ , \tag{3.15}$$

$$\frac{\partial \boldsymbol{B}}{\partial t} - \frac{1}{a} \boldsymbol{\nabla} \times (\boldsymbol{v} \times \boldsymbol{B}) = -\frac{\dot{a}}{2a} \boldsymbol{B} \ , \tag{3.16}$$

$$\boldsymbol{\nabla} \cdot \boldsymbol{B} = 0 \ , \tag{3.17}$$

where ρ the comoving density, p is the comoving gas pressure, $\boldsymbol{v}$ is the proper peculiar velocity, $\boldsymbol{B}$ is the comoving magnetic field, e is the total peculiar energy per unit comoving volume, $\tilde{p}$ is the total comoving pressure, γ is the ratio of the specific heats, Φ is the proper peculiar gravitational potential from both dark matter and baryons, $a = 1/(1 + z)$ is the expansion factor related to the redshift z, and t denotes the time.

By setting $a = 1$, $\dot{a} = 0$ and $\ddot{a} = 0$, this system of equations can be applied in case of non-cosmological conditions.

The comoving total fluid energy density E is given by:

$$E = \left(e - \frac{\rho |\boldsymbol{v}|^2}{2} - \frac{|\boldsymbol{B}|^2}{2} \right) \ , \tag{3.18}$$

The total comoving isotropic pressure $\tilde{p}$ is given by:

$$\tilde{p} = p + \frac{B^2}{2} \ , \tag{3.19}$$

where p is the thermal pressure.

The system of equations is complete with an equation of state (Eq. 3.9) and the poisson equation (Eq. 3.3).

In this formulation, the comoving quantities that are evolved by the solver are related to the proper observable quantities by the following equations:

$$\boldsymbol{x}_{\text{proper}} = a\boldsymbol{x} \; , \tag{3.20}$$

$$\boldsymbol{v}_{\text{proper}} = \boldsymbol{v} + \dot{a}\boldsymbol{x} \; , \tag{3.21}$$

$$\rho_{\text{proper}} = \rho a^{-3} \; , \tag{3.22}$$

$$p_{\text{proper}} = p a^{-3} \; , \tag{3.23}$$

$$\Phi_{\text{proper}} = \Phi - \frac{1}{2}a\ddot{a}\boldsymbol{x}^2 \; , \tag{3.24}$$

$$\boldsymbol{B}_{\text{proper}} = \boldsymbol{B} a^{-3/2} \; , \tag{3.25}$$

$$E = a^3 \left(E_{\text{proper}} - \dot{a}\boldsymbol{x} \cdot \boldsymbol{v}_{\text{proper}} - \frac{1}{2}\dot{a}^2\boldsymbol{x}^2 \right) \; . \tag{3.26}$$

3.2 Generating initial conditions

The team of the Cosmic Background Explorer (COBE) firstly discovered in in 1992 the anisotropy in the cosmic microwave background radiation (e.g. [3]). With superior angular resolution, the NASA Wilkinson Microwave Anisotropy Probe (WMAP) mapped the CMB temperature anisotropy over the whole sky (e.g. [4]). The Planck mission improved on WMAP and reduced the uncertainties due to dust contamination owing to its ten times better sensitivity and two times better angular resolution (e.g. [5]). These observations showed that the Universe was almost homogeneous with very small density perturbation.

Tiny variations in the density of matter in the early universe leave an imprint in the CMB in the form of temperature fluctuations from point to point across the sky. The red spots are the hot regions corresponding to low density with temperature 2.7251K and the blue regions corresponding to high density are the cold regions with temperature 2.7249K (see Fig. 3.1). Thus, the fluctuations in temperature are 0.0002 K and the perturbation in density is 1 in 100000.

We need to assign initial conditions to perform our computations. For this reason, we adopt the mathematical/cosmological model ΛCDM, which introduces three major components of the universe are the dark energy included as a cosmological constant Λ, cold dark matter (CDM) and ordinary matter. The main parameters of this model are given by very precise measurements taken from observations of the CMB by WMAP and PLANCK. The parameters of the ΛCDM model, from the planck collaboration release [43], are summarized in Table 3.1. The Ω-parameters are ratios with the critical density $\rho_{\text{c}} = 9.47 \times 10^{-27} \, \text{kg m}^{-3}$. Ω_{m} is the mass density including the baryon mass and the dark matter, Ω_{Λ} is effective mass density of dark energy described as cosmological constant, Ω_{b} is the baryon mass density. In addition, the Hubble constant (h) in units of $100 \, \text{km s}^{-1} \, \text{Mpc}^{-1}$. In addition, the power spectrum, given by eisenstein1999, assumes a spectral in-
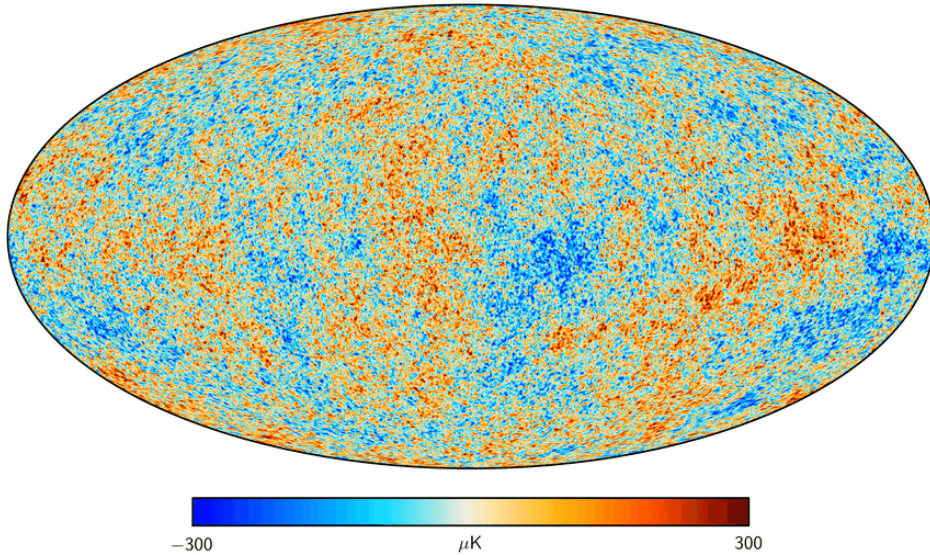
Figure 3.1: All-sky map of the CMB temperature as obtained by Planck. The blue regions are cold representing the high density region, while the red regions are hot representing the low density region.

dex (n) normalized to σ_8. This normalization has been increased to compensate for the relatively small box size and account for structure that might otherwise have been missed (see table 1 in [70]).

Ω_m	Ω_Λ	Ω_{b}	h	σ_8	n
0.2603	0.6911	0.0486	0.6774	1.2	0.961

Table 3.1: The cosmological parameters used to generate the initial conditions, calibrated from the most recent CMB observations.

The initial conditions were generated by implementing the parameter into the so-called "MUSIC code" [175]. In this way, the density distribution, the velocity dispersion of the particles and the computational box setup will be available.

This step would generate a unigrid simulation which means a computational box with no nested grids, i.e. the grids are uniformly distributed in the computational box. The initial conditions are adopted in ENZO to perform the numerical computations to reach the collapse. In post-processing the results, we find the position of the minihalo in which there is a formation of a star. We then calculate the initial Lagrangian volume centred on this halo which we choose it to be a sphere with a radius of $4r_{\mathrm{vir}}$. Using MUSIC again to generate new zoom-in initial conditions that has one nested grid around this Lagrangian volume.

The simulations are initialized with a $0.2 \, \mathrm{Mpc}/h$ comoving box on a side at $z = 100$, with a base resolution of 256^3 using the initial state as shown in Fig. 3.2.
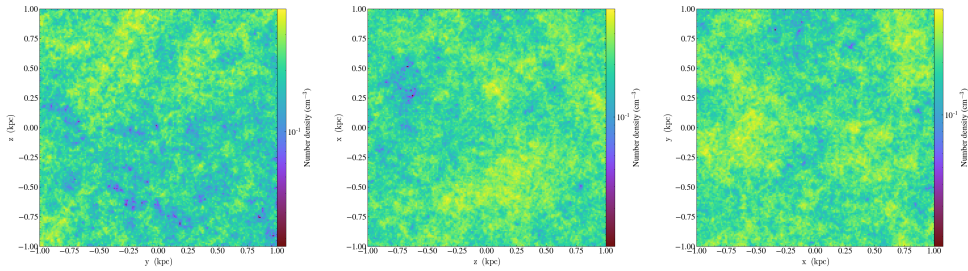
Figure 3.2: The initial number density distribution at redshift $z = 100$, given from the mathematical model ΛCDM model, calibrated to high precision from the CMB observations. The cosmological box was initially almost homogeneous with very small density perturbation.

We refine the grid on baryon and dark matter overdensities of $3 \times 2^{-0.2l}$, where l is the AMR level. The exponent is chosen, so that the refinement becomes super-Lagrangian and the cells are refined more aggressively. We also always resolve the local Jeans length by 64 cells to avoid artificial fragmentation during gaseous collapse. If any of these criteria are met in a single cell, it is flagged for further spatial refinement. We stop the simulation when the maximum density reaches $10^{15} \, \text{cm}^{-3}$ at maximum level of refinement of 25, equivalent to a special resolution of $4 \times 10^{-5} \, \text{pc}/h$ in the comoving system.

3.3 Thermodynamics treatment

3.3.1 Primordial chemical network

The present calculation makes use of the three-dimensional code "Enzo" released by [174]. This code has the advantage of combining an N-body solver with adaptive mesh hydrodynamics, within the context of cosmological initial conditions. We introduce several modifications, suitable for our project, such as additional stability requirements to treat strong shocks and rarefaction waves.

It is essential to include the chemistry and radiative cooling in modeling star formation. Forming stars wouldn't be possible if the the gas was unable to cool. Otherwise, the pressure of the plasma will be in equilibrium with gravity and no collapse would take place. Hence, there is a need for a physical process that makes the plasma lose energy. This process is the radiative cooling. In the formation of the Pop III stars, strong shocks heat the collapsing gas to the virial temperature at the virial radius. Radiative cooling will allow the gas to collapse and form stars at the center of the dark matter minihalos (e.g. [11]). The virial temperature of the halo is derived by assuming that the gravitational potential energy of the halo is twice its kinetic energy, given in Eq. (2.4).

To study the chemical and thermal evolution of the gas, the non-equilibrium

$$
\begin{array}{rcl}
\text{H} + \text{e}^- & \rightarrow & \text{H}^+ + \text{e}^- + \text{e}^- \\
\text{H}^+ + \text{e}^- & \rightarrow & \text{H} + \gamma \\
\text{He} + \text{e}^- & \rightarrow & \text{He}^+ + \text{e}^- + \text{e}^- \\
\text{He}^+ + \text{e}^- & \rightarrow & \text{He} + \gamma \\
\text{He}^+ + \text{e}^- & \rightarrow & \text{He}^{++} + \text{e}^- + \text{e}^- \\
\text{He}^{++} + \text{e}^- & \rightarrow & \text{He}^+ + \gamma \\
\text{H} + \text{H} & \rightarrow & \text{H}^+ + \text{e}^- + \text{H} \\
\text{H} + \text{He} & \rightarrow & \text{H}^+ + \text{e}^- + \text{He} \\
\text{H} + \gamma & \rightarrow & \text{H}^+ + \text{e}^- \\
\text{He} + \gamma & \rightarrow & \text{He}^+ + \text{e}^- \\
\text{He}^+ + \gamma & \rightarrow & \text{He}^{++} + \text{e}^-
\end{array}
$$
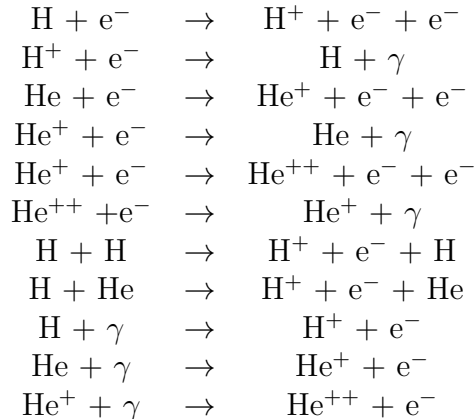
Table 3.2: Chemical reactions linking H, H^+, He, He^+, He^{++} and e^-, namely collisional excitation, collisional ionization, recombination and photoionization heating of H, He and He^+.

chemistry is solved using the `Grackle`[2] chemistry library [176]. The following 12 primordial species are included: H, H^+, H^-, H_2, H_2^+, He, He^+, He^{++}, D, D^+, HD, e^-, by setting `MultiSpecies = 3`. These species are linked by 35 reactions. In table 3.2, the chemical reactions linking the Hydrogen and Helium are summarized. These include the photoionization reactions of H and He, as well as the recombination of H^+, He^+ and He^{++} and the collisional ionization of H by collisions with H and He atoms. Table 3.3 presents the chemical reactions involving the molecular hydrogen H_2 and the ions responsible for its formation H^-, H_2^+. These include the dissociation and formation of molecular hydrogen via the H^- and H_2^+ channels, and also via three-body reactions. It is well-known that the H_2 formation process is sensitive to the three-body reaction rates [177]. We specifically choose the rates given in [66]. Table 3.4 lists the chemical reactions involving Deuterium namely D, D^+ and HD. These reactions allow to accurately trace the HD abundance, since HD can become a more effective coolant than H_2 in cold gas [77].

In the present calculations, a modified version of the `Grackle` chemistry library (e.g. [176]) is employed to solve the non-equilibrium chemistry network of the 12 primordial species (H, H^+, H^-, H_2, H_2^+, He, He^+, He^{++}, D, D^+, HD, e^-). These species are linked by 33 reactions including the formation of molecular hydrogen via the H^- and H_2^+ channels [47], and also via three-body reactions. In addition, the key cooling and heating processes are incorporated, such as H_2 ro-vibrational transitions, chemical heating and induced emission. It is well-known that the H_2 formation pathway is sensitive to the three-body reaction rate (e.g. [177]), with a concomitant impact on the Pop III star formation process. The specific rate employed in these simulations is the one given in [66].

---

[2]https://grackle.readthedocs.io/

$$
\begin{aligned}
\text{He}^+ + \gamma &\rightarrow \text{He}^{++} + \text{e}^- \\
\text{H} + \text{e}^- &\rightarrow \text{H}^- + \gamma \\
\text{H}^- + \text{H} &\rightarrow \text{H}_2 + \text{e}^- \\
\text{H} + \text{H}^+ &\rightarrow \text{H}_2^+ + \gamma \\
\text{H}_2^+ + \text{H} &\rightarrow \text{H}_2 + \text{H}^+ \\
\text{H}_2 + \text{H}^+ &\rightarrow \text{H}_2^+ + \text{H} \\
\text{H}_2 + \text{e}^- &\rightarrow \text{H} + \text{H} + \text{e}^- \\
\text{H}_2 + \text{H} &\rightarrow \text{H} + \text{H} + \text{H} \\
\text{H}^- + \text{e}^- &\rightarrow \text{H} + \text{e}^- + \text{e}^- \\
\text{H}^- + \text{H} &\rightarrow \text{H} + \text{e}^- + \text{H} \\
\text{H}^- + \text{H}^+ &\rightarrow \text{H} + \text{H} \\
\text{H}_2^+ + \text{e}^- &\rightarrow \text{H} + \text{H} \\
\text{H}_2^+ + \text{H}^- &\rightarrow \text{H}_2 + \text{H} \\
\text{H} + \text{H} + \text{H} &\rightarrow \text{H}_2 + \text{H} \\
\text{H} + \text{H} + \text{H}_2 &\rightarrow \text{H}_2 + \text{H}_2 \\
\text{H}^- + \gamma &\rightarrow \text{H} + \text{e}^- \\
\text{H}_2^+ + \gamma &\rightarrow \text{H} + \text{H}^+ \\
\text{H}_2 + \gamma &\rightarrow \text{H}_2^+ + \text{e}^- \\
\text{H}_2^+ + \gamma &\rightarrow \text{H}^+ + \text{H}^+ + \text{e}^- \\
\text{H}_2 + \gamma &\rightarrow \text{H} + \text{H} \\
\text{H} + \text{H} + \text{grain} &\rightarrow \text{H}_2 + \text{grain}
\end{aligned}
$$
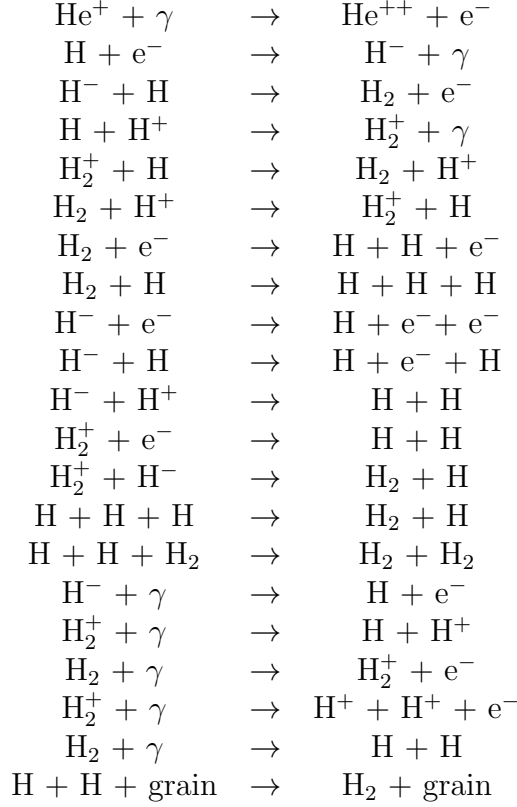
Table 3.3: The new chemical reactions added when considering H^-, H_2 and H_2^+ describing the formation and destruction of molecular hydrogen, the most important coolant in primordial gas.

$$
\begin{aligned}
\text{H}^+ + \text{D} &\rightarrow \text{H} + \text{D}^+ \\
\text{D}^+ + \text{H} &\rightarrow \text{H} + \text{D}^+ \\
\text{H}_2 + \text{D}^+ &\rightarrow \text{HD} + \text{H}^+ \\
\text{HD} + \text{H}^+ &\rightarrow \text{H}_2 + \text{D} \\
\text{D} + \text{H}^- &\rightarrow \text{HD} + \text{e}^-
\end{aligned}
$$

Table 3.4: Chemical reactions including Deuterium, describing the formation and destruction of the second cooling agent HD.

`Grackle` evolves the Lagrangian energy equation and solves the stiff network of coupled chemical rate equations with a low-order backwards difference formula (BDF) approach, due to its stability and ease of implementation [178]. With the total cooling and heating rates in hand, we can write:

$$\frac{\mathrm{d}e}{\mathrm{dt}} = -\dot{e}_{\mathrm{cool}} + \dot{e}_{\mathrm{heat}} \ . \tag{3.27}$$

Here, e is the specific internal energy, related to temperature via $e = k_{\mathrm{B}}T/[(\gamma - 1)\mu m_{\mathrm{H}}]$, with k_{B} being the Boltzmann constant, μ the mean molecular weight, and m_{H} the mass of a hydrogen atom.

The integrator is sub-cycled according to a time-step constraint, to enhance accuracy:

$$\Delta t \leq 0.1 \frac{e}{\dot{e}} \ . \tag{3.28}$$

To solve the rate of change for a given chemical species, the creation and destruction rates are grouped as follows:

$$\frac{\partial n_{\mathrm{i}}}{\partial t} = C_{\mathrm{i}}(T, n_{\mathrm{j}}) - D_{\mathrm{i}}(T, n_{\mathrm{j}})n_{\mathrm{i}} \ , \tag{3.29}$$

where C_{i} is the total creation rate of the i-th species for a given temperature T and the abundances of the other species. The second term on the right-hand side of Eq. (3.29) is the destruction rate of the given species.

The key cooling and heating processes included in Grackle are H_2 rotational transitions, H_2 radiative cooling, HD cooling, chemical heating and collisionally induced excitation of H_2 at high densities.

We also include the impact of chemical heating or cooling due to the formation or destruction of molecular hydrogen. For H_2 destruction, we remove 4.48 eV per H_2 molecule dissociated. In addition, at very high densities, when the H_2 lines become optically thick, the H_2 cooling rate decreases using a density-dependent opacity correction term as in [85].

3.3.2   Adjustment of the optical depth

In order to reach the stage of protostar formation, the collapse should be followed till a density $n \gtrsim 10^{20}\,\mathrm{cm^{-3}}$, where the primordial gas becomes opaque to its cooling radiation [64]. I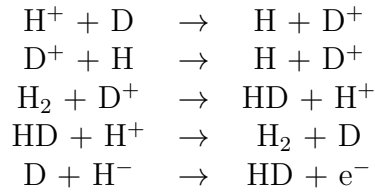t was possible to achieve such density in few calculations [70] with cosmological simulations of extreme dynamical range. Still, the challenge is to follow the accretion process onto the growing core for $\sim 10^4\,\mathrm{yr}$, which correspond to the Kelvin-Helmholtz timescale during the evolution of stars (e.g. [179]).

A problem arises with adjusting the explicit time step according to the "Courant condition" (see [180]). A compromise is widely used by introducing sink particles at relatively low density [181]. Another approach is based on escape probability

method combined with the Sobolev approximation to treat the complex radiative transfer of partially opaque H_2 line cooling (e.g. [52,55,81]).

We here adopt the alternative approach of [158], who introduced an artificially stiffened equation of state at a threshold density, n_{th}, chosen for reasons of computational expediency. This stiffening is implemented through an artificially imposed optical depth at $\sim n_{th}$, resulting in an artificial hydrostatic core inside the collapsing minihalo. This artificial core is larger and more massive than the true protostellar core, representing the resolution limit of the simulation. In this work, the radiative cooling for gas elements with density exceeding a threshold number densities of $n_{th} = 10^{12}\,\mathrm{cm}^{-3}$ is reduced. At number densities $n_H \gtrsim 10^{12}\,\mathrm{cm}^{-3}$, the primordial gas begins to become optically thick to H_2 line emission, but other cooling channels, such as collision-induced emission, will remain effective until much higher densities [180], beyond our artificial threshold density. We therefore do not accurately resolve the star formation process on the smallest scales. Specifically, we impose an artificial optical depth via [158]:

$$\tau_{art} = \left(\frac{n_H}{n_{th}}\right)^2 \, . \tag{3.30}$$

The corresponding escape fraction is:

$$\beta_{esc,art} = \frac{1 - \exp\left(-\tau_{art}\right)}{\tau_{art}} \, . \tag{3.31}$$

All radiative cooling rates are reduced by this factor. This treatment has the advantage that the complicated hydrodynamics inside the opaque core does not need to be followed. Similarly, solving the energy and chemical rate equations at the increasingly high densities beyond the resolution scale is now avoided, replaced by a simple adiabatic evolution.

To test for numerical convergence, we consider select cases with an increased threshold number density of $n_{th} = 10^{15}\,\mathrm{cm}^{-3}$. We evolve these high-resolution runs as far as computationally possible, given the now much shorter required Courant time steps. To approximately account for the increased optical depth of the primordial gas to H_2 line cooling in the high-resolution runs at $n \gtrsim 10^{12}\,\mathrm{cm}^{-3}$ [67,80], the H_2 cooling rate is decreased by a density-dependent term in `Grackle`, as expressed in eq. 19 in [85].

Determining the extent of the protostar in simulations that do not insert sink particles can be achieved by finding the photospheric surface of the protostar, where the optical depth reaches unity (e.g., fig. 9 in [182]). In our present treatment, the size of the central core corresponds to the surface where the opacity is unit, i.e. where the number density reaches the threshold density of $n_{th} = 10^{12}\,\mathrm{cm}^{-3}$. Again, we emphasize that we here cannot resolve the true protostar, in terms of mass and radius, and this should be kept in mind when considering the resulting fragment masses and mass distribution, discussed below.

3.4 Incorporating MHD effects

3.4.1 Methodology

For each grid cell, the code `Enzo` solves the equations describing the internal gas energy and the total energy, as a function of time. This dual energy formalism ensures that the method yields the correct entropy jump at strong shocks, and also delivers accurate pressures and temperatures in cosmological hypersonic flows. For the runs without magnetic fields (hereafter termed hydro runs), the Piecewise Parabolic Method (PPM) is used (e.g. [183]). On the other hand, to solve the cosmological MHD equations (e.g. [174]), the Harten-Lax-van Leer (HLL) Riemann solver is employed (e.g. [184]). The solenoidal constraint $\boldsymbol{\nabla} \cdot \boldsymbol{B} = 0$ is enforced according to the Dedner scheme (e.g. [185]).

Since the formation of the first stars in the Universe is investigated in the present work, the Lyman-Werner (LW) radiation background is not included in the present simulations, since the LW photons with energies just below the H-ionizing threshold would otherwise act to photo-dissociate H_2, the main cooling agent in primordial gas, at subsequent stages of cosmic star formation (e.g. [186]). Therefore, H_2 self-shielding does not need to be included as well.

When performing our MHD calculations, the amplification of the seed magnetic field to its fully-developed asymptotic strength is not treated in a self-consistent way. This has been attempted in [18], who found that the amplification process cannot be resolved accurately, due to the extreme dynamic range of the turbulent cascade involved. We therefore carry out a suite of numerical experiments, where we *assume* that small-scale turbulent dynamos have amplified the fields to close to equipartition with the turbulent kinetic energy (e.g. [136, 154]). We also consider cases where subsequent large-scale kinematic dynamo action has established a large-scale, ordered field configuration (e.g. [88]). Thus, it is reasonable to insert an already fully developed magnetic field into the simulation box, if the number density exceeds $10^8 \, \mathrm{cm^{-3}}$ with an amplitude to be discussed next.

3.4.2 Field amplitude

An important question concerns the expected field strengths in Pop III star forming regions? The inspection of relevant results, according to [130], reveal that the Biermann battery in conjunction with compressional amplification can result in fields with strengths of $B = 10^{-9} \, \mathrm{G}$ at number density $n = 10^{10} \, \mathrm{cm^{-3}}$ at the center of a cosmological halo where a Pop III star is expected to form. Hence, the magnetic fields created by the Biermann battery are dynamically unimportant at all densities below $n = 10^{10} \, \mathrm{cm^{-3}}$, where the ratio of thermal gas to magnetic pressure is $\beta = P_{\mathrm{th}}/P_{\mathrm{B}} \geq 10^{15}$ at all times during the evolution of the minihalo.

However, significantly larger field strengths are reached when dynamo activity is considered. In fact, [160] showed that the small-scale dynamo increases the turbulent magnetic field to the level of 1 to 10 percent of equipartition, in agreement with [142, 143]. The authors in [153] and [137] also noted that once the field reaches equipartition, it will remain there as the collapse continues, so that the field will increase as $\rho^{1/2}$ (for a constant turbulent velocity) rather than the $\rho^{2/3}$ behaviour for compressional amlification under flux freezing. In [89], the field actually achieved equipartition at number density $10^{12}\,\mathrm{cm}^{-3}$, and half the equipartition at the number density $10^{8}\,\mathrm{cm}^{-3}$, where magnetic fields are introduced in our simulations.

When inserting the fields in our calculation, we specifically assume that the magnetic energy is nearly in equipartition with the thermal energy of the gas, such that (e.g. [187]):

$$\frac{B_{\mathrm{sat}}^2}{8\pi} = \eta\, c_{\mathrm{s}}^2\, \rho \,, \tag{3.32}$$

where c_{s} is the sound speed, ρ the local gas density of the cell, and η a free parameter describing the coupling efficiency in the range 0 and 1. We consider three values $\eta = 0.1$, 0.5 and 0.9, to denote cases of weak, intermediate and strong fields, respectively. Hence, in our calculations, we clearly assess the importance of MHD effects on Pop III protostar formation under different field strengths.

3.4.3   Field geometry

In carrying out our suite of numerical experiments, we consider several illustrative configurations for the magnetic field geometry: uniform, radial, toroidal and poloidal, each with the three values of η discussed above. In addition, we also consider a random field configuration, corresponding to a situation where the large-scale organization of the small-scale turbulent fields did not occur. For our adopted approach, the magnetic field is added locally in cells at every timestep, where the density exceeds $10^{8}\,\mathrm{cm}^{-3}$, providing three-dimensional Cartesian components.

With the magnitude, $B = B_{\mathrm{sat}}$, given by Eq. (3.32), we can specify our selected field configurations, projected onto the Cartesian grid. The uniform field has equal components along the $x, y,$ and z axes, such that:

$$\mathbf{B}_{\mathrm{uniform}} = \frac{B}{\sqrt{3}}(\hat{\mathbf{i}} + \hat{\mathbf{j}} + \hat{\mathbf{k}}) \,, \tag{3.33}$$

where $\hat{\mathbf{i}}, \hat{\mathbf{j}},$ and $\hat{\mathbf{k}}$ are the unit vectors in Cartesian coordinates. This field has the straightforward configuration of parallel, equidistant and equal vectors throughout the disk.

A radial field is also considered, as follows:

$$\mathbf{B}_{\mathrm{rad}} = -B\left(\frac{x}{r}\,\hat{\mathbf{i}} + \frac{y}{r}\,\hat{\mathbf{j}} + \frac{y}{r}\,\hat{\mathbf{k}}\right) \,, \tag{3.34}$$
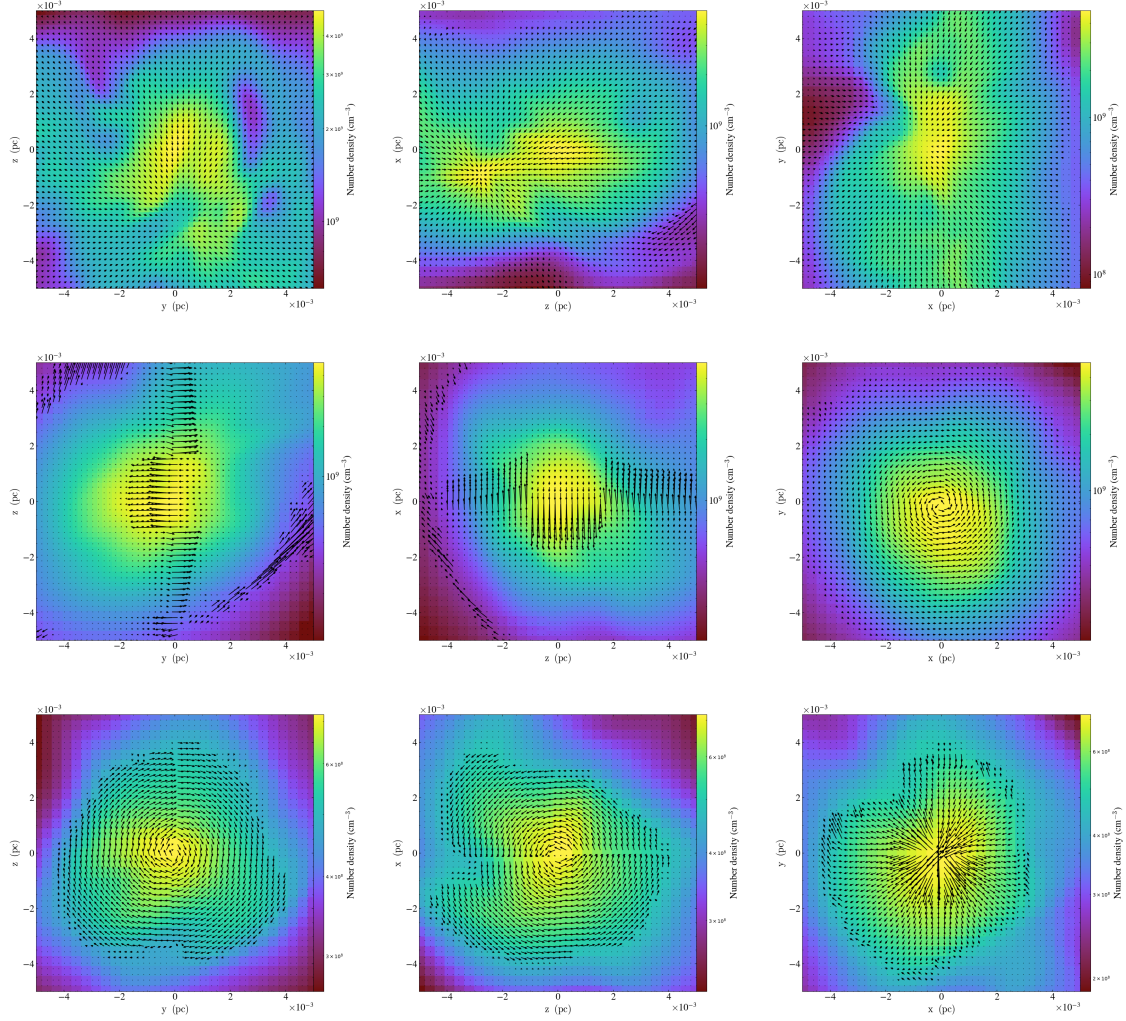
Figure 3.3: Initial magnetic field configurations given in Eq. (3.33)-(3.36). *First row:* Radial field for intermediate strength case (RI), equal vectors pointing towards the highest density cell. *Second row:* Toroidal field (TI), spinning around the z axis. *Third row:* Poloidal field (PI), along the azimuth in spherical coordinates.

where coordinates are expressed with respect to the location of the maximum density, and $r = (x^2 + y^2 + z^2)^{1/2}$ is the radius. By construction, the position of the density maximum is excluded ($r \neq 0$), such that the field remains divergence-free. This field, visualized in the first row of Fig. 3.3, points radially toward the densest cell.

In order to define the toroidal and poloidal fields, we use spherical coordinates (r,θ,ϕ), with $\hat{\mathbf{r}}$, $\hat{\boldsymbol{\theta}}$ and $\hat{\boldsymbol{\phi}}$ representing the corresponding unit vectors. The polar and azimuthal angles are as usual given via:

$$\theta = \arccos \frac{z}{r} \; ,$$
$$\phi = \arctan \frac{y}{x} \; . \tag{3.35}$$

The toroidal field has a component only along $\hat{\boldsymbol{\phi}}$, when considering the canonical toroidal-poloidal field decomposition, which again has to be projected onto the Cartesian system to be implemented in `Enzo`:

$$\mathbf{B}_{\mathrm{tor}} = B \left(-\sin\phi \, \hat{\mathbf{i}} + \cos\phi \, \hat{\mathbf{j}} \right) \; . \tag{3.36}$$

This field in spinning around the $\hat{\mathbf{k}}$ axis, hence does not have a component along this axis, as is shown in the second row of Fig. 3.3.

Similarly, the poloidal field has a component only along $\hat{\boldsymbol{\theta}}$, which can be written in Cartesian coordinates as:

$$\mathbf{B}_{\mathrm{pol}} = B \left(\cos\theta \, \cos\phi \, \hat{\mathbf{i}} + \cos\theta \, \sin\phi \, \hat{\mathbf{j}} + \sin\theta \, \hat{\mathbf{k}} \right) \; . \tag{3.37}$$

The poloidal field spins around the $\hat{\mathbf{j}}$, and $\hat{\mathbf{k}}$ axes (see third row in Fig. 3.3.) It's also useful to note that both the toroidal and poloidal fields are divergence-free per construction.

Finally, in the random field case, the three Cartesian coordinates of $\mathbf{B}_{\mathrm{random}}$ are taken to be B_{sat}, given in Eq. (3.32), where η is now generated randomly between 0 and 1, separately in every cell. This is in contrast to the other geometries, where η takes specific values, as discussed above (Sec. 3.4.2). This mimics in a rough way the small-scale turbulence during the amplification of the field.

CHAPTER 4

RESULTS

We compare the results of all the runs at the time when the maximal density reaches $\rho_{\mathrm{max}} = 10^{12}$ cm^{-3} and 10^{15} cm^{-3} [188]. We call the simulations as the correspond to the applied geometry of the magnetic field: UI for uniform, RI for radial, PI for poloidal, TI for toroidal, with intermediate field strength. Another letter is also used to indicate the magnitude of the field: L for the low magnetic field case and H for the high magnetic field. In addition, the case without magnetic field is called HD and the case with randomized magnetic field is called Rand.

4.1 Global properties of collapse

4.1.1 Dark matter minihalos

At a redshift $z \sim 25$, the adopted box in the present calculations contains multiple minihaloes, able to host dense baryonic cores. The lowest-mass halo that is marginally able to trigger the collapse of the primordial gas has a minimum mass of about 2.3×10^5 $M_\odot$. However, the most massive minihalo has a mass of $M_{\mathrm{halo}} = 1.2 \times 10^6 M_\odot$ and a virial radius of $r_{\mathrm{vir}} = 130$ pc (for these characteristics, see Sect. 2.2.1).

The minihalo with the maximum mass as indicated above is the main concern of the present work, because of the highest density achieved in such halo.

The baryonic gas collapses into a web-like structure, shown in the left panel of Fig. 4.1. The minihalos, visualized over the density distribution, are numbered based on their mass, as noted above. The minihalo of maximum mass, shown in the right panel of Fig. 4.1, encloses the peak density investigated below.
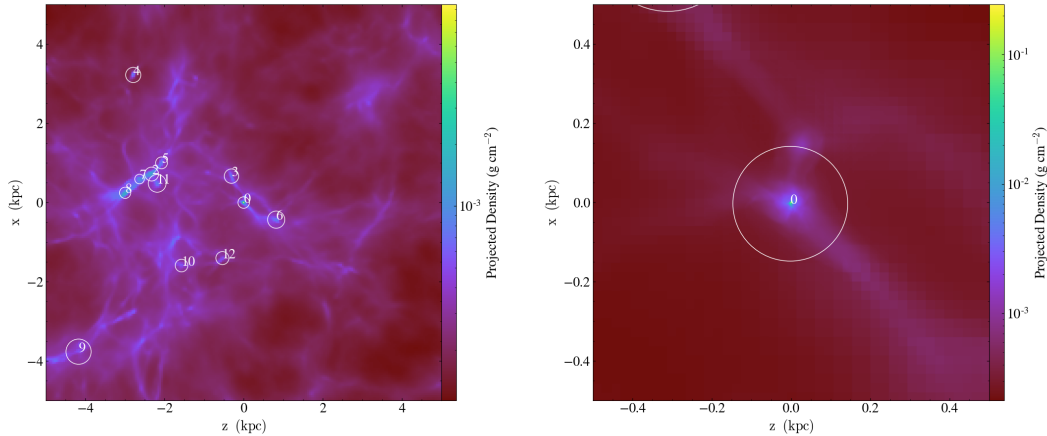
44

Figure 4.1: Distribution of the gas density around the central peak, with dark matter minihalos. The minihalos are numbered with decreasing mass, minihalo 0 being the most massive. *Left panel:* A zoom-out realization with side length 10 *kpc*. *Right panel:* A zoom-in realization with side length 1 *pc*. The gas collapses into a web-like structure inside these dark matter minihalos. The most massive minihalo hosts the density peak investigated in this work.

4.1.2 Evolution of the magnetic field

The magnetic field was introduced as diskussed in Sec. 3.4. Its magnitude increases toward the center of the gas cloud as shown in Fig. 4.2, while maintaining the constraint $\nabla \cdot \mathbf{B} = 0$. We emphasize that this constraint was best maintained with the toroidal field.

To evaluate the importance of the magnetic field during the collapse, it is useful to investigate the ratio of the kinetic to magnetic pressure $\beta = P_{\text{th}}/P_{\text{B}}$. As diskussed in Sec. 2.2, in the calculations of [130], β was greater than 10^{15} throughout the collapse, and this led to the conclusion that the magnetic field is unimportant. The left panel of Fig. 4.3 shows this ratio as a function of radius for the high-resolution poloidal and toroidal geometries with intermediate strength. It is seen that the toroidal field has the biggest impact of the collapse since β is two orders of magnitude larger than that of the poloidal field. In addition, we conducted a series of numerical calculations incorporating magnetic field from the beginning, similar to [130]. The initial seed field strengths were adequately chosen to be $B_{\text{i}} = 10^{-12}$, 10^{-10} and 10^{-8} G. The ratio β is shown in the right panel of Fig. 4.3, from which we can conclude that for these initial seeds the magnetic field will also be important in the collapse. Another comment is that the behavior of β in case of the toroidal and poloidal fields is similar to the $B_{\text{i}} = 10^{-8}$ G and 10^{-10} G case, respectively.

45
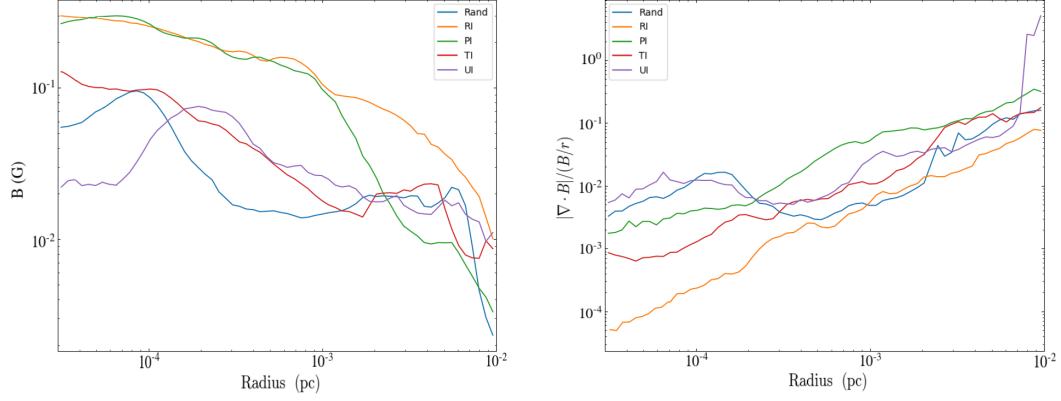
Figure 4.2: Magnetic field properties in the centre of the star formation region, evaluated when the gas density reaches a maximum value of 10^{15} cm^{-3}. *Left panel:* Magnitude of the magnetic field, according to Equ. (3.32) with $\eta = 0.5$, as a function of the distance to the central peak for different field geometries, as indicated. *Right panel:* Magnetic field divergence versus radius with the best result in case of the toroidal field.
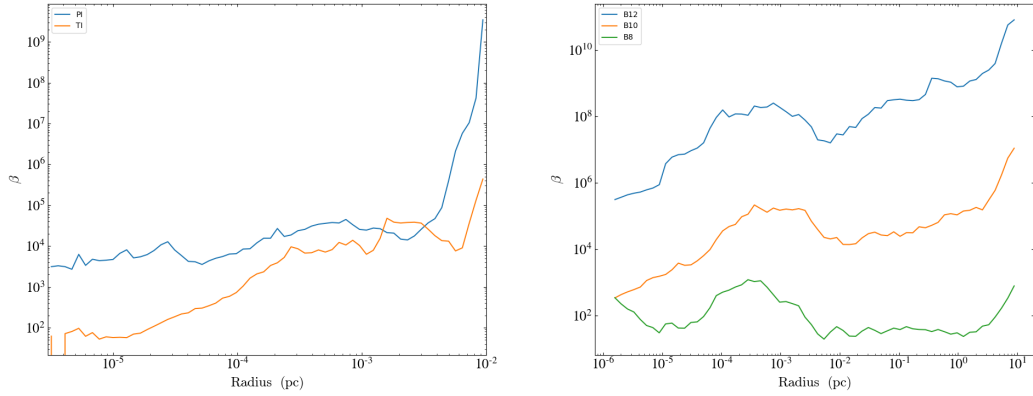
Figure 4.3: The ratio of kinetic to magnetic pressure as a function of radius, evaluated when the gas density reaches a maximum value of 10^{15} cm^{-3}, *Left panel:* For the high-resolution calculations with intermediate fields as indicated. *Right panel:* For a magnetic field introduced in the beginning of the numerical calculation, with strengths $B_i = 10^{-12}$ G (B12), $B_i = 10^{-10}$ G (B10) and $B_i = 10^{-8}$ G (B8).

4.1.3 Morphology of the disk

The first difference between the HD and the MHD cases is the delay of the collapse, of 0.1 Myr. This was expected due the impact of the magnetic pressure. What really distinguishes the simulation including MHD from those with HD is the impact on the evolution of the collapsing gas, especially when the number density exceeds $10^8\,\mathrm{cm}^{-3}$. For example, the time to reach a density of $10^{12}\,\mathrm{cm}^{-3}$ took 15 kyr in the HD case, but 20 kyr in the MHD case with intermediate strength of the magnetic field.

In Fig. 4.4, we compare evolutionary sequences for the HD and select MHD cases at three maximum densities: $10^9\,\mathrm{cm}^{-3}$, $10^{12}\,\mathrm{cm}^{-3}$ and $10^{15}\,\mathrm{cm}^{-3}$. In each case, we find a central object surrounded by a well-organized disk. The ensuing evolution leads to multiple fragmentation of the disk as seen in the middle panel of Fig. 4.4. However, in the HD case at the latest calculated stage a radially symmetric disk with little remaining substructure around it (see top right panel). But this will change with a better resolution as will be shown in Fig. 4.5. In the case with TI, two clumps temporarily emerge (middle panel), which merge into one central object by the end of the simulation, but the surrounding disk is deformed now. As we shall see in Fig. 4.5, the effect of the magnetic field is to inhibit fragmentation, most effectively in case of the TI-field.

Another result of the present investigation is that the field with low-η the change of geometry had little effect on the morphology of the disk. In contrast, the highest η-cases independent of geometry lead to a thinner and less dense disk, which inhibits star formation.

It is intriguing to compare the HD case with the TI one for different spatial scales. This is done in Fig. 4.5, where views of the central morphology are shown for three box sizes, 0.1 pc, 0.01 pc and $5 \times 10^{-4}\,\mathrm{pc}$. In the TI-case, the central core is more compact with elongated disk, and this is in contrast to the symmetric disk in the HD-case. The most remarkable difference in the morphology between the HD and the MHD cases is evident in the third column with the smallest spatial scale. Several clumps are found in the HD-case. In contrast, only one central peak is formed in the TI case. The dynamics inside this photosphere surface, not reliably resolved here, will be investigated further in the high-resolution runs, employing a threshold number density for the modified optical depth in equation (3.30), set to the much higher $n_{\mathrm{th}} = 10^{15}\,\mathrm{cm}^{-3}$ (as diskussed in Sec. 3.3.2).

Finally, in case of the UI-field, the disk has a sort of radial symmetry, unlike the axisymmetric disk of the toroidal geometry.

In the high-resolution runs, the maximal number density reached is $n_{\mathrm{max}} = 2 \times 10^{15}\,\mathrm{cm}^{-3}$, for the HD, PI and TI cases. Hence, even though the true protostellar stage (n $\sim 10^{21}\,\mathrm{cm}^{-3}$) was not achieved yet in our simulation, due to limited computational resources, we get somewhat closer with minimal approximations (see [70]). In Fig. 4.6, we show the number density distribution for the HD case
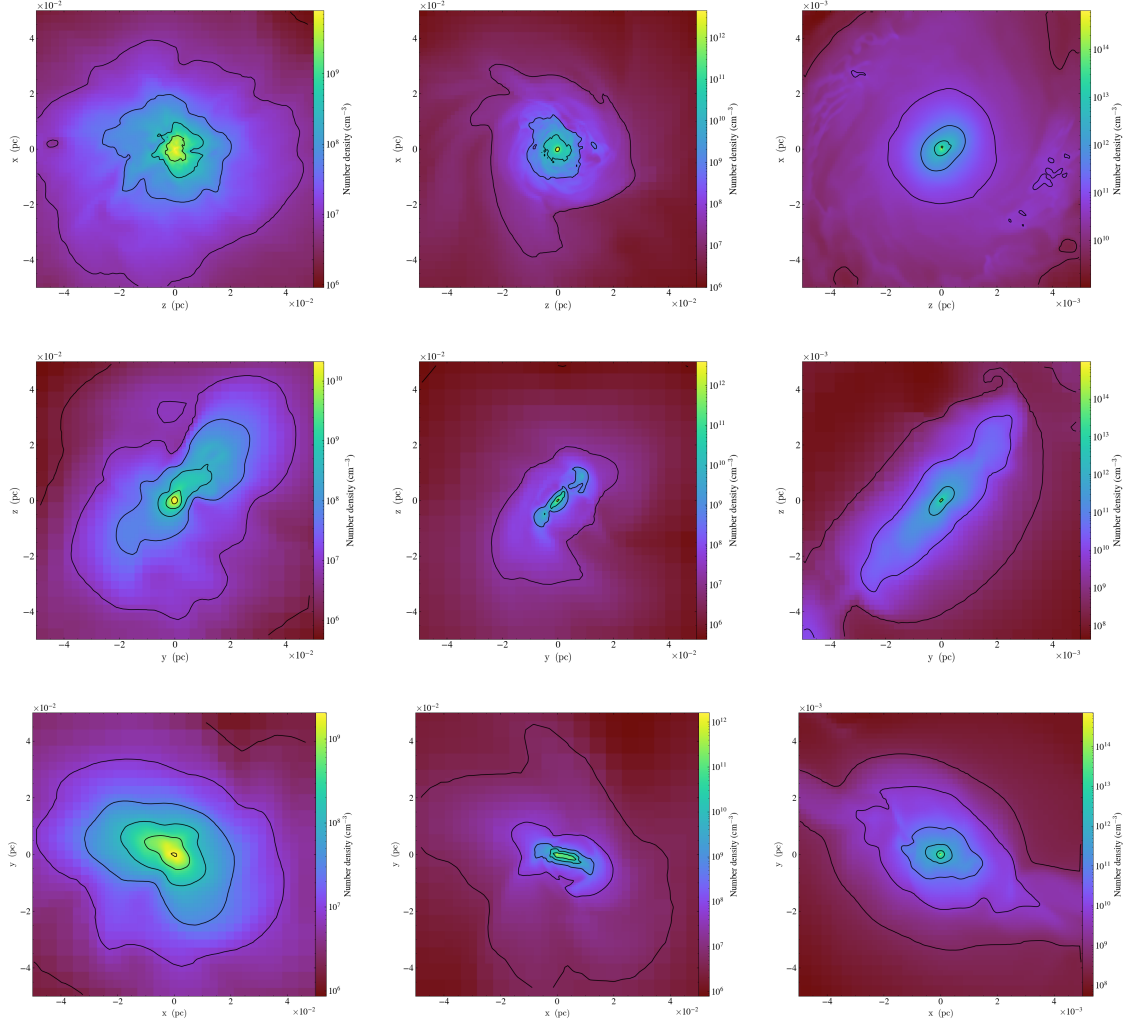
Figure 4.4: Time evolution of the gas distribution around the central clump. Shown are three rows, the first corresponds to the HD case, the second to toroidal magnetic field (TI), and the third to the uniform magnetic field (UI). The columns correspond to the number densities $10^9 \, \text{cm}^{-3}$, $10^{12} \, \text{cm}^{-3}$ and $10^{15} \, \text{cm}^{-3}$. Note that the first column is showing the stage at which the magnetic field has been initialized. See text for details.
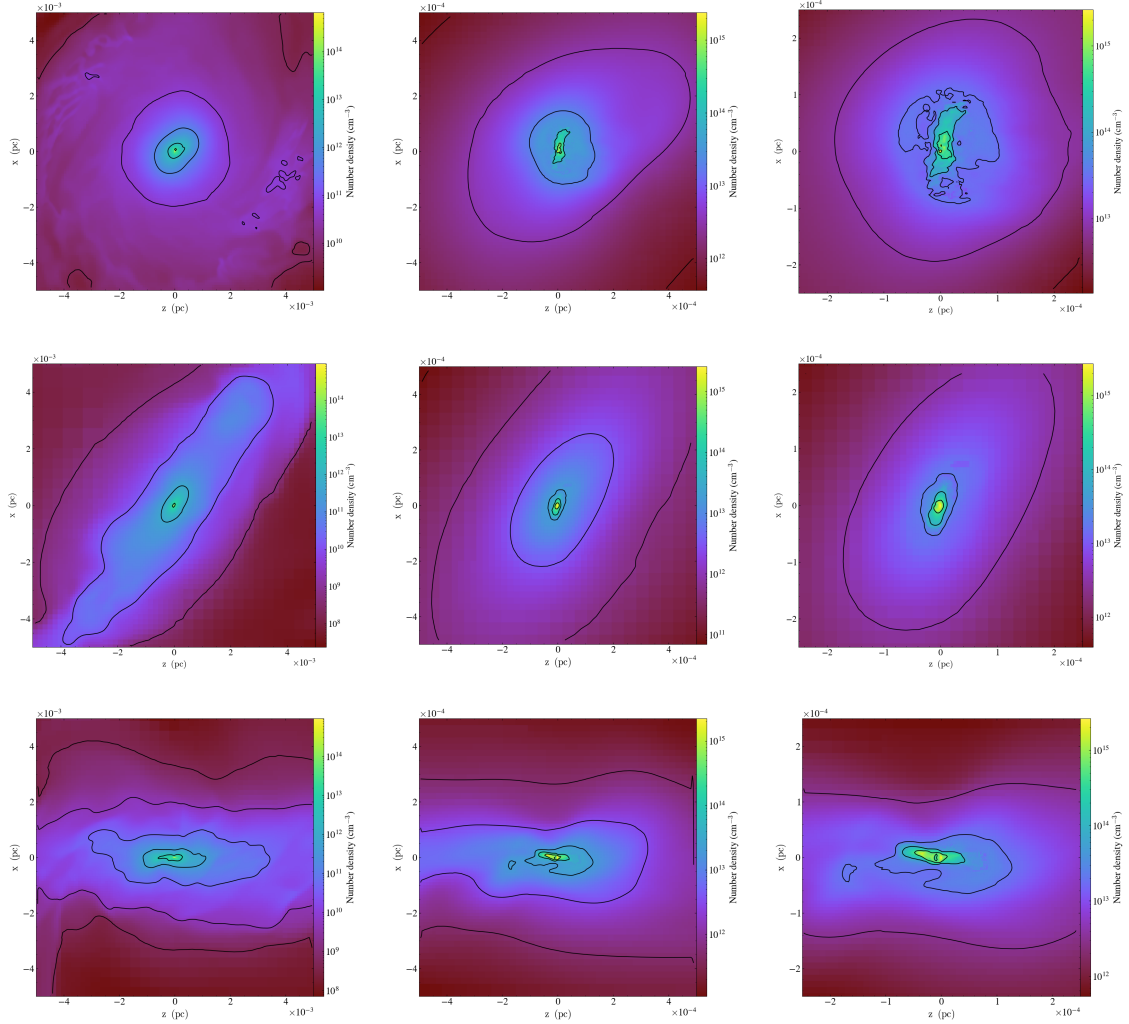
Figure 4.5: Density distribution around the maximum density of $10^{15}\,\mathrm{cm^{-3}}$, to compare the final stage at different spatial scales. *First row:* HD case. *Second row:* Toroidal field for intermediate magnitude (TI). *Third row:* Poloidal field for intermediate magnitude (PI). Boxes of different lengths around the central peak are displayed: *Left column:* $0.01\,\mathrm{pc}$. *Middle column:* $0.1\,\mathrm{pc}$. *Right column:* $5 \times 10^{-4}\,\mathrm{pc}$, showing the situation inside the protostellar surface. This zoom-in indicates that the central peak in the HD case looks clumpy, in contrast to the TI-case, that forms only one core and the PI-case that shows two clumps. However, such small scales are not reliably resolved here, and will be investigated further below in the high-resolution runs.

49
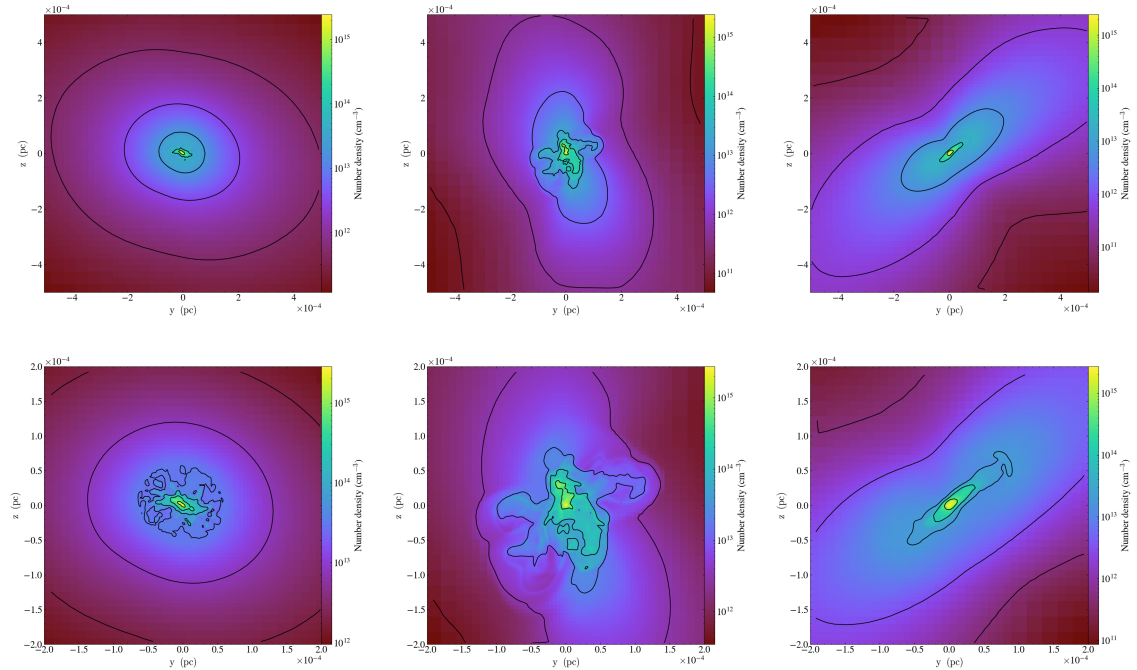
Figure 4.6: Density distribution at the final time for the high-resolution runs. *First column:* HD case. *Second column:* Poloidal field for intermediate strength case (PI). *Third column:* Toroidal field for intermediate strength case (TI). These calculations prove that the clumpiness of the disk in the HD case shown in Fig. 4.5 is not a numerical artifact. In addition, the toroidal field has clearly the biggest impact on the morphology of the central core, implying that the geometry of the field affects the fragmentation of the disk.

(left column), the PI-case (middle column) and the TI-case (right column) at the final time reached in each case. It is noticeable that the clumpiness of the disk in the HD case is still visible in the high-resolution, implying that the morphology seen in the first row panel of Fig. 4.4 is not a numerical artifact. Moreover, similar to third row in Fig. 4.4, in the PI-case the disk formed two fragments close to the central core. In contrast, the TI-case forms a single central core. This again proves that the toroidal configuration has the strongest effect on inhibiting the fragmentation of the disk.

4.1.4 Thermodynamics considerations

Basic insight in thermodynamics is essential to understand the process of star formation in general and the formation of the first stars in particular. Several issues are involved, such as the temperature variation with density, radiative cooling and heating processes (compressional and shock heating). In Fig. 4.7, we compare the HD-case with the TI-case. It is seen that both HD and TI-cases

exhibit very similar behavior for $n < 10^8 \, \mathrm{cm^{-3}}$. Beyond this number density, temperatures reach somewhat lower values in the MHD case. The reason is that magnetic pressure is countering the collapse, thus reducing the compressional heating. We note that the different geometries of the magnetic field do not noticeably affect the overall thermodynamic evolution.
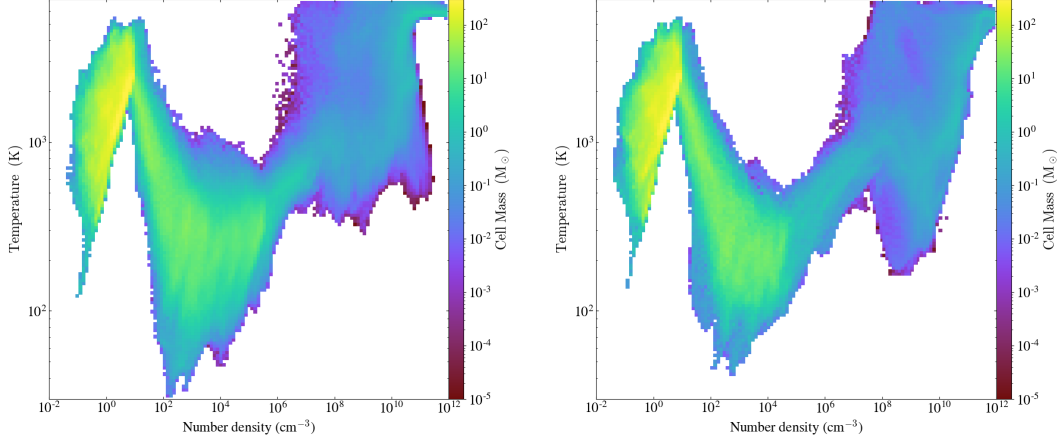
Figure 4.7: The temperature profiles in the HD case (left panel) and the MHD case (right panel) when the maximum density reaches $10^{12} \, \mathrm{cm^{-3}}$.
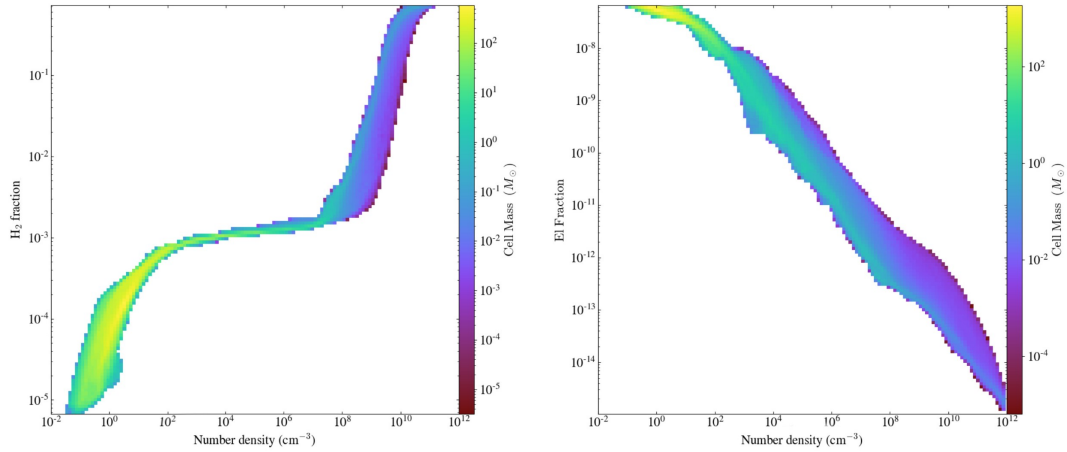
Figure 4.8: The H_2 fraction (left panel) and the electrons fraction (right panel) profiles, in the HD case, when the maximum density reaches $10^{12} \, \mathrm{cm^{-3}}$.

The overall evolution of the temperature and the fractions of molecular hydrogen and free electrons, as seen in Fig. 4.8, depict the history of the collapse. The temperature increases initially in the range up to $n = 1 \, \mathrm{cm^{-3}}$ due to compressional heating of the collapsing gas. And this is accompanied with the formation

of H_2 molecules via the H^- channel [76]. This molecular fraction reaches a value of $f_{H_2} = 10^{-3}$ capable of ensuing cooling to temperature decrease to a minimum of $\sim 200 - 300\,K$ at $n = 10^4\,cm^{-3}$. This corresponds to what is often termed the characteristic, or 'loitering' state [50]. Towards higher densities, the transition to rotational level leads to less efficient H_2 cooling under local thermodynamic equilibrium conditions (LTE), so that gradual increase of temperature occurs due to the continuing gravitational collapse. At $n = 10^8\,cm^{-3}$, the three-body reactions become effective enhancing the formation of H_2 molecules [66], thus converting the primordial gas into a fully molecular phase. Due to the boost in cooling, another (local) temperature minimum is achieved, but the compressional heating succeeds to rise the temperature again (e.g. [73]).

The relative temperature suppression by the magnetic field, discussed above, can also be seen in Fig. 4.9, where we show the radial temperature profile for selected cases. The temperature decrease close to the centre, seen in all cases, is a numerical artifact due to the extrapolated stiffened equation of state that artificially slows down compressional heating in the central region. The temperature increases to a maximum of $\simeq 6000\,K$ in the HD case, but not in the MHD case where the maximum temperature reached is $\simeq 5500\,K$, since magnetic pressure counteracts the collapse for the MHD runs. We emphasize again that the various magnetic field geometry has a minor change on the resulting thermal profiles. The evolution beyond the numerical threshold density, n_{th}, cannot be resolved here, rendering the approach to the final hydrostatic core inaccessible (see [52, 70]).
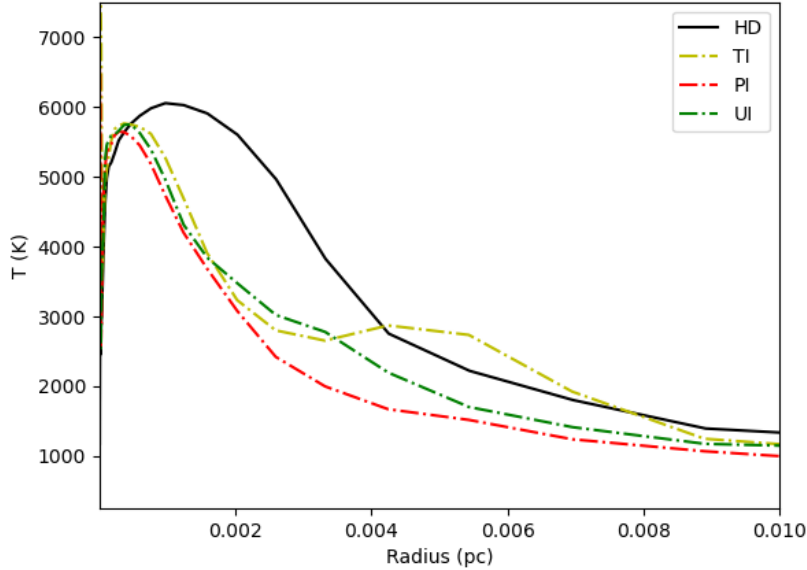
Figure 4.9: Temperature profile as a function of distance from the central peak at density $10^{15}\,\mathrm{cm^{-3}}$. Cases with different magnetic field geometries for intermediate initial strength are compared to the HD case, as indicated. As can be seen, the magnetic field leads to overall lower temperatures in the disk, due to the added magnetic pressure that delays the collapse. The central drop in temperature is a numerical artifact (see Sec. 4.1.4).

4.1.5 Kinematics

In terms of the resulting kinematics, our simulations indicate that the infall velocity is greater in the HD case than in the MHD cases, reflecting the role of the magnetic field in slowing the collapse, as shown in Fig. 4.10. The square of the vorticity, defined by $\omega = \boldsymbol{\nabla} \times \boldsymbol{v}$, describes the local spinning motion of the gas. Its maximal value at the center indicates that the latter exhibits high turbulent energy. Furthermore, we note that the radial Mach number is subsonic in the HD case, whereas in the MHD cases the disks are approaching transonic conditions. Finally, we point out that the angular momentum transport is more efficient in the TI-case than in the HD case, as indicated in the steep decline of the angular momentum profile (see bottom-left panel in Fig. 4.10).

Figure 4.10: The radial velocity, the vorticity squared, the radial mach number and the angular momentum magnitude profiles as a function of radius for different cases of magnetic field strengths and geometries when the maximum density reaches 10^{15} cm^{-3}.

4.2 Fragmentation properties

The stability of the disk is an important aspect of the collapse, studied by evaluating the Toomre parameter Q [189], given by:

$$Q = \frac{c_s \kappa}{\pi G \Sigma} \; , \tag{4.1}$$

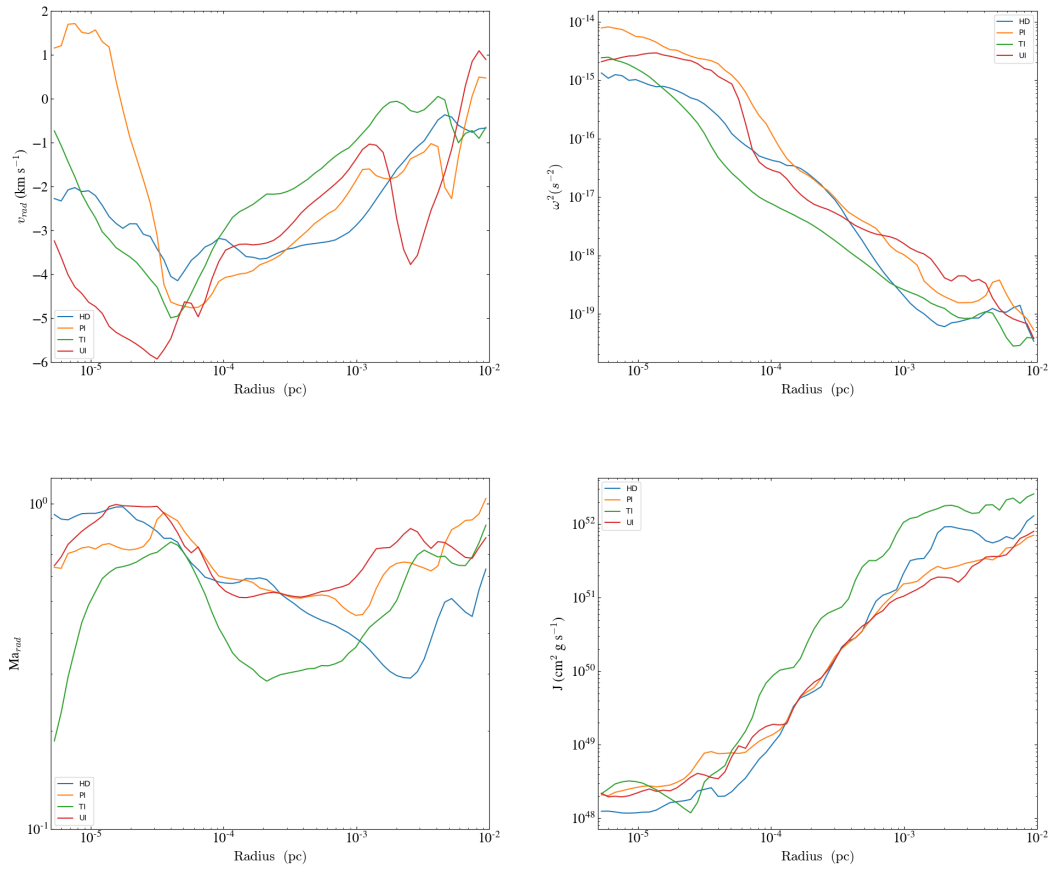where c_s is the sound speed of the gas, κ is the epicyclic frequency of the disk, Σ the surface density. This parameter determines whether perturbations in an infinitely thin, isothermal disk can grow. The authors in [70] replaced κ by the orbital frequency Ω.

To evaluate this stability criterion, three timescales are particularly important: the free-fall timescale t_{ff}, the time it takes the sound waves to cross a flattened system t_{sound} and the timescale for shear motion to tear the system apart t_{shear}, given by:

$$t_{ff} = \sqrt{\frac{3\pi}{32 G \rho}} \; , \tag{4.2}$$

$$t_{sound} = \frac{H_p}{c_s} \; , \tag{4.3}$$

$$t_{shear} = \frac{d}{v_{shear}} \; , \tag{4.4}$$

where H_p being the pressure scale height and d the overall scale of the collapsing region.

In order for the gas to collapse, the free-fall timescale should be smaller than t_{sound} and t_{shear}. We can construct a combined criterion via:

$$t_{ff}^2 < t_{sound} t_{shear} \; . \tag{4.5}$$

This condition for gravitational collapse results in:

$$\frac{c_s v_{shear}/d}{\pi G \rho H_p} < \frac{32}{3\pi^2} \sim 1 \; , \tag{4.6}$$

The left hand side of Eq. 4.6 is equivalent to the known expression of the Toomre parameter given in Eq. 4.1, since the term ρH_p represents the surface density Σ, the shear velocity can be taken to be the rotational velocity around the disk centre $v_{shear} \to v_{rot}$, the fragmentation scale is comparable to the radial distance from the centre $d \to R$, then $v_{shear}/d \to v_{rot}/R = \Omega$.

Furthermore, by assuming the thin disk approximation, the pressure scale height is described as $H_p \sim R c_s/v_{rot} = c_s/\Omega$. Our local stability parameter (Eq. 4.6) then becomes as given in Eq. (23) in [158]:

$$Q_{local} \sim \frac{\Omega^2}{\pi G \rho} \; . \tag{4.7}$$
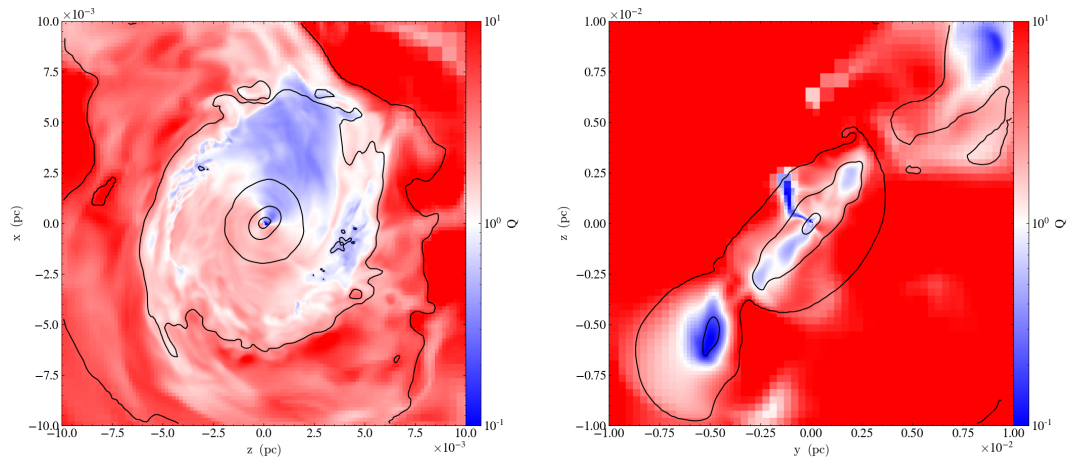
Figure 4.11: Local Toomre stability criterion Q around the central peak at the final time when the maximal density is 10^{15} cm^{-3}. *Left panel:* HD case. *Right panel:* Intermediate-strength toroidal field case (TI). Several small unstable clumps in the HD case around the radially symmetric center, in contrast to two unstable clumps close to central elongated disk in the TI-case.

The inspection of Fig. 4.11 reveals the following. The central configurations are morphologically different. The disk in the HD case is radially symmetric, while the symmetry is broken in the MHD (TI) case, with a dominant elongated structure. In the HD case, several clumps are embedded in the disk, emerging ~ 100 AU away from the central density peak (left panel). In the TI-case, there are two dominant clumps along the elongated structure. We conclude that the magnetic field suppresses fragmentation into low-mass clumps by increasing the pressure-support against gravity.

To accurately describe the state of this ongoing sub-fragmentation, merging, and possibly ejection of fragments is beyond the reach of our current simulation, as it would require higher resolution extended for significantly longer periods of time.

4.3   Resulting masses of the fragments

Another crucial property of the first stars is their mass distribution, or initial mass function (IMF). We first inspect the masses of the disks as a function of radius in Fig. 4.12, a comparison is done between the HD-case and different magnetic field configurations using initial intermediate strength. It turns out that the toroidal field formed the most massive core, followed by the radial field. Otherwise, the magnetic field did not affect the mass distribution in the disk. Moreover, the total mass in the sphere of radius 10^{-2} pc was changed by a factor of about 2.

As presented in Sec. 3.4, the protostar was defined by its blackbody photo-
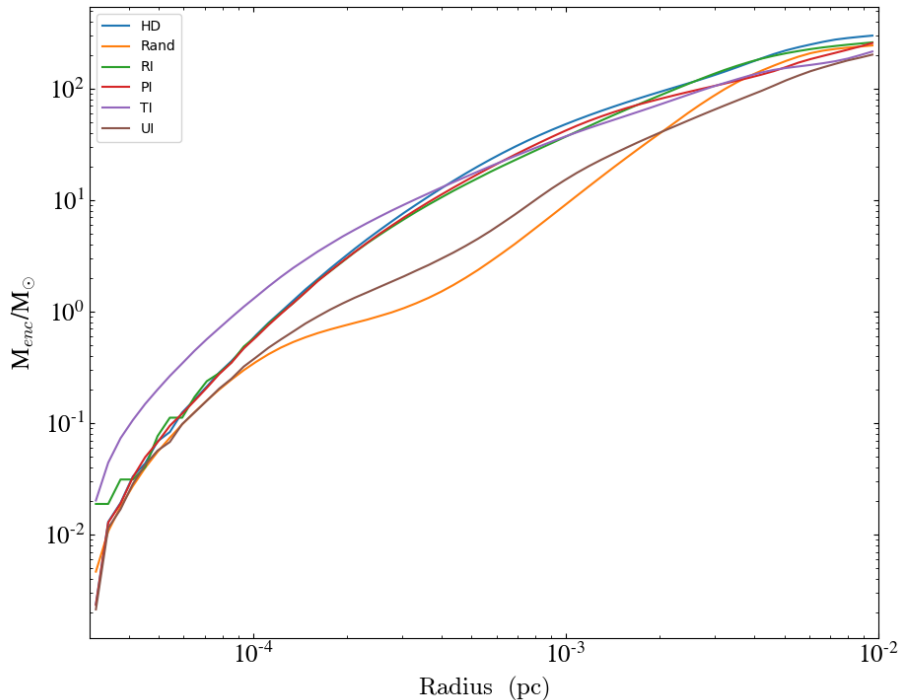
Figure 4.12: Enclosed mass in a sphere of radius 10^{-2} pc around the central density peak, as a function of radius for the HD and select MHD cases, specifically the Random, RI, TI, PI and UI configurations, when the maximum density reaches $10^{12}\,\mathrm{cm}^{-3}$. The toroidal field configuration leads to the formation of the most massive core, followed by the radial configuration.

sphere at an optical depth of $\tau = 0.63$ corresponding to the adopted threshold number density $n_{\mathrm{th}} = 10^{12}\,\mathrm{cm}^{-3}$ for the modified optical depth. Fig. 4.13 shows the extent of the central object, at $n_{\mathrm{th}} = 10^{12}\,\mathrm{cm}^{-3}$. Concerning the masses of these central objects, our result, as far as our calculations tell, are given in Table 4.1. The increase of the masses depends on the achieved density and the accretion rate. Since the magnetic field leads to a decrease of the accretion rate, higher density is needed to find the final mass of the protostar. The accretion rate found $(0.001 - 0.1\ M_\odot/\mathrm{yr})$ is compatible with [70].

As for the high-resolution calculations, where the threshold number density is increased to $n_{\mathrm{th}} = 10^{15}\,\mathrm{cm}^{-3}$, the extent of the central object with the modified photosphere as described above is visualized in Fig. 4.14 in the cases as indicated there. The masses of the resulting central objects are given in table 4.2. Based on these results, we find that the magnetic field leads to more massive cores, when the resolution is sufficient. This effect was missed in the medium-resolution runs.
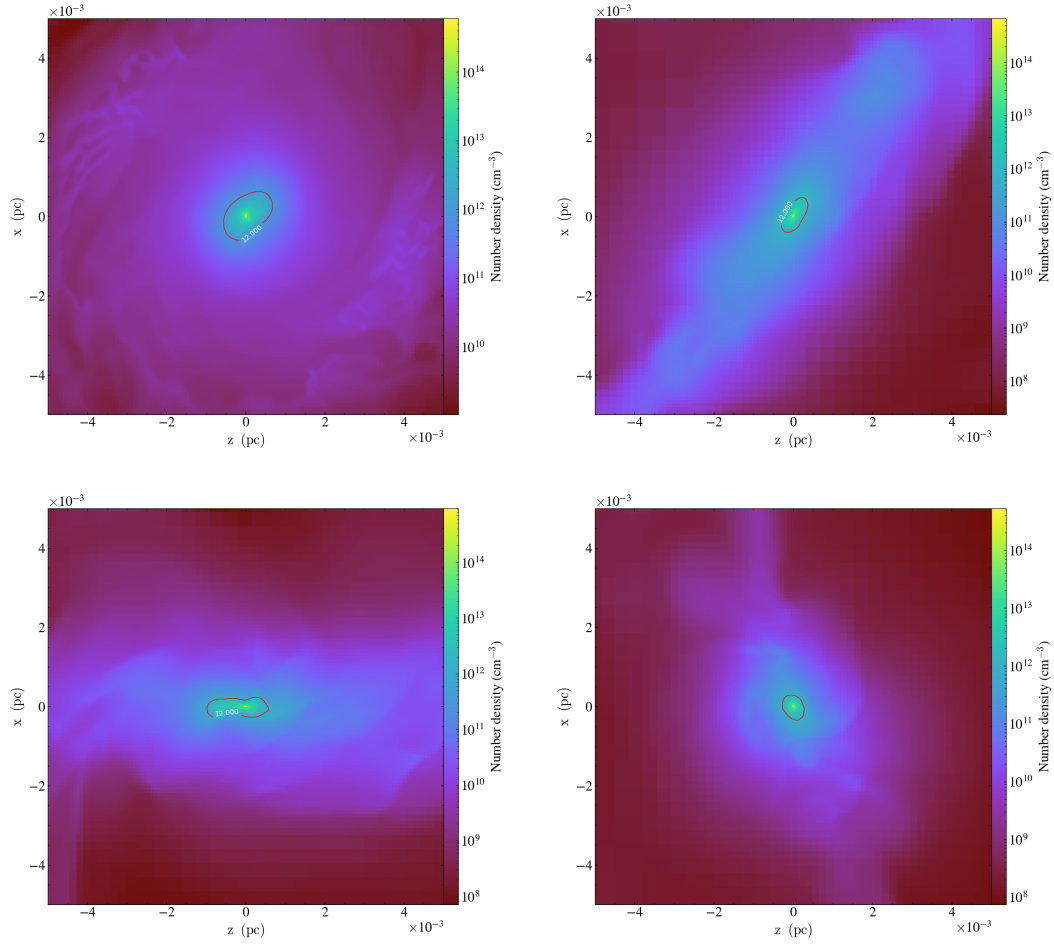
Figure 4.13: Extent of the central core defined by its photospheric surface, where the threshold number density for the modified optical depth is $n_{th} = 10^{12}\,\text{cm}^{-3}$. *Top left panel:* HD case. *Top right panel:* Toroidal field for intermediate strength case (TI). *Bottom left panel:* Poloidal field for intermediate strength case (PI). *Bottom right panel:* Uniform field for intermediate strength case (UI).

Case	M_1 ($M_\odot$)	M_2 ($M_\odot$)	t_{acc} (yr)	$\dot{M}_*$ ($M_\odot/yr$)
HD	17.9	30.6	72	0.177
TI	7.9	12.0	66	0.062
PI	18.1	19.0	52	0.017
UI	1.2	17.5	1020	0.016

Table 4.1: The masses (M_1) of the main central core, defined by the photospheric surface, when the maximum density is $10^{12}\,\mathrm{cm}^{-3}$, the masses ($M_2$) at density $10^{15}\,\mathrm{cm}^{-3}$, the corresponding accretion time, t_{acc}, and the accretion rate, $\dot{M}_*$. Displayed are the HD, toroidal, poloidal and uniform magnetic field cases with intermediate-strength normalization. The somewhat reduced accretion rates are caused by the magnetic field for all geometries considered.

Hence, a compromise on the resolution for reasons of computational expediency could lead to inaccurate conclusions.
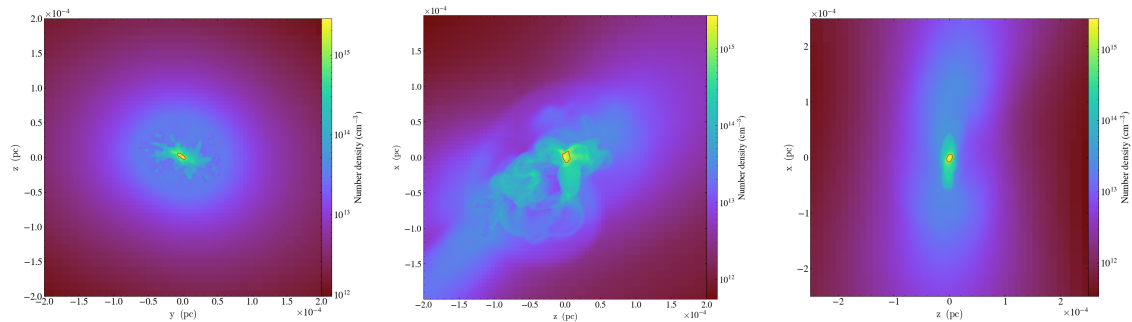
Figure 4.14: Extent of the central core defined by its photospheric surface, for the high-resolution runs, where the threshold number density for the optical depth is $n_{\mathrm{th}} = 10^{15}\,\mathrm{cm}^{-3}$. *Left panel:* HD case. *Middle panel:* Poloidal field for intermediate strength case (PI). *Right panel:* Toroidal field for intermediate strength case (TI).

Case	M_{high} ($M_\odot$)
HD	0.02
PI	0.05
TI	0.14

Table 4.2: The masses (M_{high}) of the main central core, defined by the photospheric surface, when the maximum density is $10^{15}\,\mathrm{cm}^{-3}$. Displayed are the HD, poloidal and toroidal magnetic field cases with intermediate-strength normalization. The magnetic field leads to the formation of more massive cores.
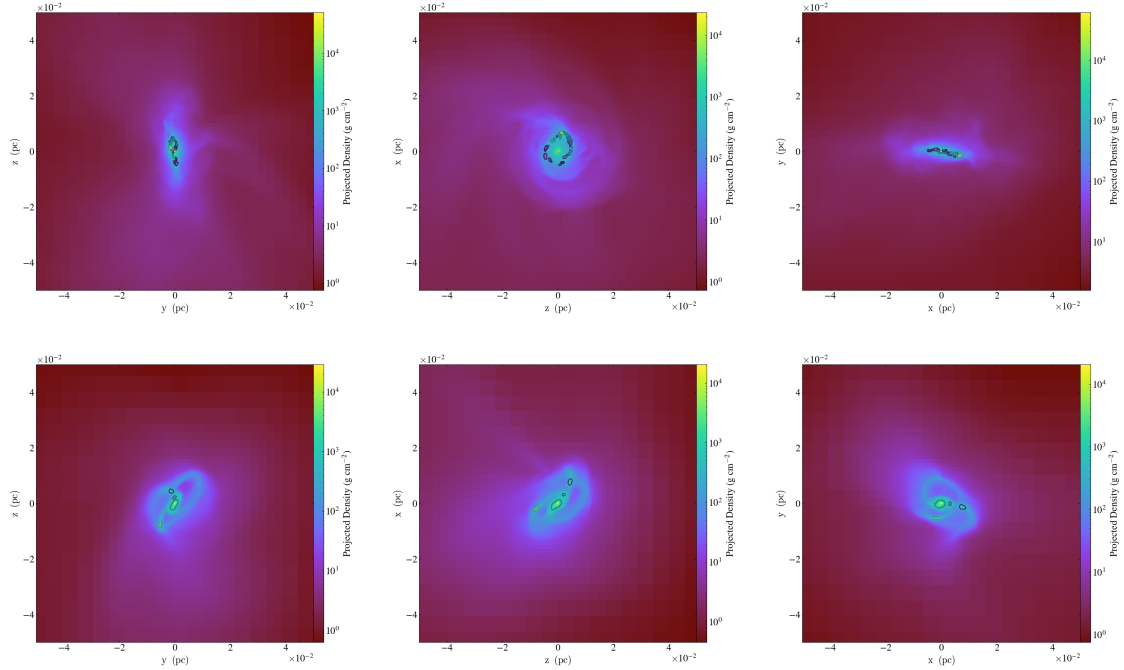
Figure 4.15: Central density projection showing the distribution of clumps. *Left panel:* HD case. *Right panel:* Intermediate-strength toroidal field case (TI). A dominant central clump is surrounded by 47 other low-mass fragments in the HD case, compared to a central clump with three smaller clumps in the MHD (TI) case.

A basic question concerns the mass distribution of the Pop III stars, or their IMF. One way to accomplish that is by identifying the cells that are gravitationally bound using the core finder as described in [190]. This routine uses a contouring algorithm that recursively identifies topologically diskonnected structures within a dataset. These cells are called a clump that would later collapse into one or several protostars. Fig. 4.15 shows snapshots of these clumps when the density is 10^{15} cm^{-3}. The first row indicates that several clumps are formed in the HD case, but only three clumps are formed in the TI-case (see second row). We see again the effect of the magnetic field inhibiting fragmentation.

To investigate the mass distribution of these clumps, we use the histogram in Fig. 4.16 taken at a density 10^{15} cm^{-3}. In the HD case, about 50 clumps emerge, with masses close to the local Jeans mass, $M_{\rm J} \sim 1 M_\odot$, as resolved in case of $n_{\rm th} = 10^{12}$ cm^{-3}. The mass distribution in this case reflects effective fragmentation of the disk. In contrast, for the MHD cases, the mass of the central clump depends on the geometry of the magnetic field. The resulting masses are 50 $M_\odot$, 10 $M_\odot$, and 15 $M_\odot$ in the PI, TI and UI cases, respectively. Furthermore, the small-mass fragments close to the resolution limit are absent in all MHD cases, as the magnetic field inhibits small-scale fragmentation. We also
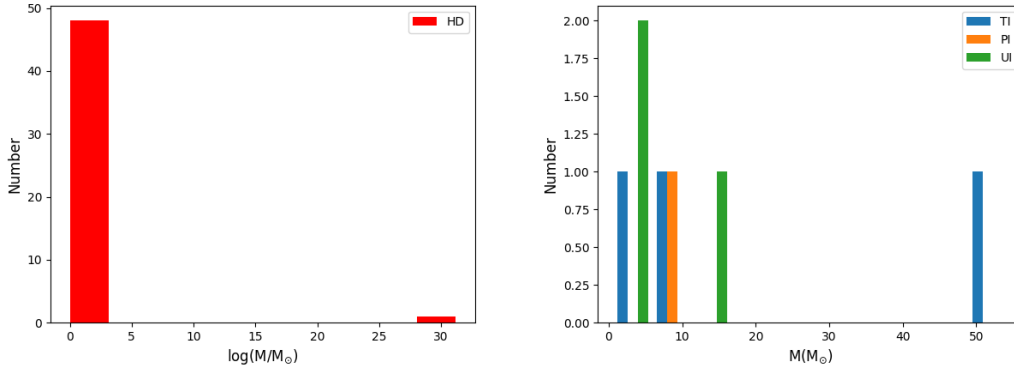
Figure 4.16: Fragment masses at density 10^{15} cm^{-3}. *Left panel:* HD case. *Right panel:* MHD cases with intermediate-strengths. One primary clump of mass of 30 $M_\odot$ is formed in the HD case, with several clumps of small masses (visualized in Fig. 4.15). In contrast, in the MHD case, only few clumps are formed, emphasizing that the magnetic field inhibits the fragmentation of the disk.

find that stronger fields lead to higher masses.

The accretion rates can be estimated from the clumps of smaller masses that accreted mass from the disk in the MHD cases. In the TI-case, these secondary clumps (shown in the second row of Fig. 4.15) have masses 7.2 $M_\odot$ and 4.4 $M_\odot$. Their respective accretion rates are 6.6×10^{-4} $M_\odot$/yr, 5.4×10^{-3} $M_\odot$/yr. While in the PI-case the accretion rate is 4.6×10^{-5} $M_\odot$/yr. These low accretion rates seem to represent the final mass of the fragments. An argument is that including the magnetic field leads to high mass Pop III stars. The accretion rate of the central core is higher than the secondary cores found above, which proves that there is a primary core that accretes more mass than the others.

CHAPTER 5

SUMMARY, CONCLUSION AND FUTURE WORK

In the present thesis project, the focus was to investigate the effect of a cosmic magnetic field on the structure and evolution of the disks and their contribution to the formation of the first stars after Big Bang, the so called Pop III stars. The process of their formation occurs under cosmological conditions, namely in minihalos of an estimated mass of $M_{\mathrm{halo}} = 1.2 \times 10^6 \ M_\odot$, with a virial radius of 130 pc, and the stage of formation is found to occur at a redshift $z = 25$. These initial conditions are based on the ΛCDM cosmological model which we have described in Sec. 3.2. The present calculations rely heavily on computational tools or numerical simulations to solve the magneto-hydrodynamic (MHD) equations which do not have analytical solutions.

To investigate the influence of the cosmic magnetic field on the evolution of the structure of the disks around the protostars, leading to the formation of Pop III stars, we have applied different configurations of the magnetic field and varied their strengths (see Sec. 3.4). In addition, we compare the results obtained from the hydrodynamic (HD) calculations with those including MHD effects.

The magnetic field was introduced in cells at a density of $10^8 \ \mathrm{cm}^{-3}$ and the computations were extended up to a density of $10^{12} \ \mathrm{cm}^{-3}$ in all cases. In addition up to a density of $10^{15} \ \mathrm{cm}^{-3}$ in the both the HD-case and MHD-case with an intermediate strength of the magnetic field. The main results of the present work are summarized as follows.

1. The different geometries applied for the magnetic field configuration have a significant effect on the resulting collapse and fragmentation of the disks. High resolution is essential to allow reasonable conclusions.

2. An important and robust result of the present investigation is the role of the initial toroidal (TI) magnetic field inhibiting disk fragmentation. In particular, a clumpy distorted disk formed in the HD case, three fragments

formed in the PI-case, while only one more massive fragment formed in the TI-case.

3. The increase in the strength of the field for the same geometry leads to a delay of the collapse.

4. We found that a strong magnetic field renders the IMF of Pop III more top-heavy.

5. The magnetic field decreases the accretion rate onto the forming protostar.

As a final remark, the present investigation was done without considering the self-consistent creation and amplification of the primordial magnetic seed field (e.g. [18, 136, 144]). We here follow [18], who argued that even with the highest resolution that is currently achievable, it is not possible to resolve the amplification of the magnetic field caused by the turbulent small-scale dynamo. Therefore, we assumed the magnitude of the field to be a fraction of its equipartition value, which has been shown to be the expected outcome of the self-consistent dynamo process (e.g. [187] and references therein). The advantage of our idealized approach is that we can carry our controlled experiments, in terms of considering a wide range of field strengths and configurations.

For future work, the effect of a toroidal field with a randomized coupling efficiency η that mimics turbulence is in preparation. Such a study is interesting because our calculations of the self-consistent amplification of an initial magnetic seed shows a toroidal configuration, in agreement with [151]. Moreover, this geometry demonstrates the biggest impact on the collapse process.

Another reflection for future work is to include resistive effects such as Ohmic and ambipolar diffusion. Even though the use of ideal MHD is justified during the early phase by the high initial degree of ionization that leads to ineffective dissipation [191], ambipolar diffusion may become important in the primordial gas when the magnetic field gets amplified to a critical strength (e.g. [152, 191]). Hence, since the current study uses ideal MHD, the inclusion of resistive effects as mentioned above should be included, especially when the collapse will be followed to higher densities. Such extension is required to draw realistic conclusions about the mass distribution of the fist stars and their resulting multiplicity.

Bibliography

[1] J. D. Bowman, A. E. E. Rogers, R. A. Monsalve, T. J. Mozdzen, and N. Mahesh, "An absorption profile centred at 78 megahertz in the sky-averaged spectrum," Nature, vol. 555, pp. 67–70, Mar. 2018.

[2] T. R. Makki, M. F. El Eid, and G. J. Mathews, "A critical analysis of the Big Bang Nucleosynthesis," *Modern Physics Letters A*, vol. 34, p. 1950194, Aug. 2019.

[3] G. F. Smoot, C. L. Bennett, A. Kogut, E. Wright, J. Aymon, N. Boggess, E. Cheng, G. De Amici, S. Gulkis, M. Hauser, *et al.*, "Structure in the cobe differential microwave radiometer first-year maps," *The Astrophysical Journal*, vol. 396, pp. L1–L5, 1992.

[4] A. Kogut, D. N. Spergel, C. Barnes, C. L. Bennett, M. Halpern, G. Hinshaw, N. Jarosik, M. Limon, S. S. Meyer, L. Page, G. S. Tucker, E. Wollack, and E. L. Wright, "First-Year Wilkinson Microwave Anisotropy Probe (WMAP) Observations: Temperature-Polarization Correlation," ApJS, vol. 148, pp. 161–173, Sept. 2003.

[5] M. Bucher, "Status of CMB Observations in 2015," in *International Journal of Modern Physics Conference Series*, vol. 43 of *International Journal of Modern Physics Conference Series*, p. 1660188, July 2016.

[6] J. H. Wise, T. Abel, M. J. Turk, M. L. Norman, and B. D. Smith, "The birth of a galaxy - II. The role of radiation pressure," MNRAS, vol. 427, pp. 311–326, Nov. 2012.

[7] S. Hirano, T. Hosokawa, N. Yoshida, H. Umeda, K. Omukai, G. Chiaki, and H. W. Yorke, "One Hundred First Stars: Protostellar Evolution and the Final Masses," ApJ, vol. 781, p. 60, Feb. 2014.

[8] A. Stacy, A. H. Pawlik, V. Bromm, and A. Loeb, "The mutual interaction between Population III stars and self-annihilating dark matter," MNRAS, vol. 441, pp. 822–836, June 2014.

[9] A. Stacy, V. Bromm, and A. Loeb, "Rotation speed of the first stars," MNRAS, vol. 413, pp. 543–553, May 2011.

[10] M. A. Alvarez, V. Bromm, and P. R. Shapiro, "The H II Region of the First Star," ApJ, vol. 639, pp. 621–632, Mar. 2006.

[11] V. Bromm, "Formation of the first stars," *Reports on Progress in Physics*, vol. 76, p. 112901, Nov. 2013.

[12] L. Haemmerlé, L. Mayer, R. S. Klessen, T. Hosokawa, P. Madau, and V. Bromm, "Formation of the First Stars and Black Holes," Space Sci. Rev., vol. 216, p. 48, Apr. 2020.

[13] R. Barkana, "The rise of the first stars: Supersonic streaming, radiative feedback, and 21-cm cosmology," Phys. Rep., vol. 645, pp. 1–59, July 2016.

[14] I. Baraffe, A. Heger, and S. E. Woosley, "On the Stability of Very Massive Primordial Stars," ApJ, vol. 550, pp. 890–896, Apr. 2001.

[15] W. W. Ober, M. F. El Eid, and K. J. Fricke, "Evolution of Massive Pregalactic Stars - Part Two - Nucleosynthesis in Pair Creation Supernovae and Pregalactic Enrichment," A&A, vol. 119, p. 61, Mar. 1983.

[16] A. Heger and S. E. Woosley, "The Nucleosynthetic Signature of Population III," ApJ, vol. 567, pp. 532–543, Mar. 2002.

[17] A. Heger, C. L. Fryer, S. E. Woosley, N. Langer, and D. H. Hartmann, "How Massive Single Stars End Their Life," ApJ, vol. 591, pp. 288–300, July 2003.

[18] M. J. Turk, J. S. Oishi, T. Abel, and G. L. Bryan, "Magnetic Fields in Population III Star Formation," ApJ, vol. 745, p. 154, Feb. 2012.

[19] M. J. Turk, J. S. Oishi, T. Abel, and G. L. Bryan, "Magnetic fields and angular momentum in population III star formation," in *First Stars IV - from Hayashi to the Future* - (M. Umemura and K. Omukai, eds.), vol. 1480 of *American Institute of Physics Conference Series*, pp. 77–80, Sept. 2012.

[20] T. Peters, P. D. Klaassen, M.-M. Mac Low, M. Schrön, C. Federrath, M. D. Smith, and R. S. Klessen, "Collective Outflow from a Small Multiple Stellar System," ApJ, vol. 788, p. 14, June 2014.

[21] J. P. Gardner and JWST Science Working Group, "The Scientific Capabilities of the James Webb Space Telescope," in *American Astronomical Society Meeting Abstracts #213*, vol. 213 of *American Astronomical Society Meeting Abstracts*, p. 426.02, Jan. 2009.

[22] M. Stiavelli, *From First Light to Reionization: The End of the Dark Ages.* John Wiley & Sons, 2009.

[23] S. R. Furlanetto, S. P. Oh, and F. H. Briggs, "Cosmology at low frequencies: The 21 cm transition and the high-redshift Universe," Phys. Rep., vol. 433, pp. 181–301, Oct. 2006.

[24] C. Kouveliotou, R. A. M. J. Wijers, and S. Woosley, *Gamma-ray Bursts.* Cambridge University Press, 2012.

[25] K. Freeman and J. Bland-Hawthorn, "The New Galaxy: Signatures of Its Formation," ARA&A, vol. 40, pp. 487–537, Jan. 2002.

[26] T. C. Beers and N. Christlieb, "The discovery and analysis of very metal-poor stars in the galaxy," *Annu. Rev. Astron. Astrophys.*, vol. 43, pp. 531–580, 2005.

[27] A. Frebel and V. Bromm, "Chemical Signatures of the First Galaxies: Criteria for One-shot Enrichment," ApJ, vol. 759, p. 115, Nov. 2012.

[28] S. s and A. Ferrara, "First stars in damped Lyα systems," MNRAS, vol. 421, pp. L29–L33, Mar. 2012.

[29] T. Nordlander, M. S. Bessell, G. S. Da Costa, A. D. Mackey, M. Asplund, A. R. Casey, A. Chiti, R. Ezzeddine, A. Frebel, K. Lind, A. F. Marino, S. J. Murphy, J. E. Norris, B. P. Schmidt, and D. Yong, "The lowest detected stellar Fe abundance: the halo star SMSS J160540.18-144323.1," MNRAS, vol. 488, pp. L109–L113, Sept. 2019.

[30] S. C. Keller, M. S. Bessell, A. Frebel, A. R. Casey, M. Asplund, H. R. Jacobson, K. Lind, J. E. Norris, D. Yong, A. Heger, Z. Magic, G. S. da Costa, B. P. Schmidt, and P. Tisserand, "A single low-energy, iron-poor supernova as the source of metals in the star SMSS J031300.36-670839.3," Nature, vol. 506, pp. 463–466, Feb. 2014.

[31] A. Frebel, E. N. Kirby, and J. D. Simon, "Linking dwarf galaxies to halo building blocks with the most metal-poor star in Sculptor," Nature, vol. 464, pp. 72–75, Mar. 2010.

[32] S. Salvadori, A. Ferrara, R. Schneider, E. Scannapieco, and D. Kawata, "Mining the Galactic halo for very metal-poor stars," MNRAS, vol. 401, pp. L5–L9, Jan. 2010.

[33] E. Caffau, P. Bonifacio, L. Sbordone, P. François, L. Monaco, M. Spite, B. Plez, R. Cayrel, N. Christlieb, P. Clark, S. Glover, R. Klessen, A. Koch, H. G. Ludwig, F. Spite, M. Steffen, and S. Zaggia, "TOPoS. I. Survey design and analysis of the first sample," A&A, vol. 560, p. A71, Dec. 2013.

[34] E. Caffau, P. Bonifacio, P. François, L. Sbordone, L. Monaco, M. Spite, F. Spite, H.-G. Ludwig, R. Cayrel, S. Zaggia, F. Hammer, S. Randich, P. Molaro, and V. Hill, "An extremely primitive star in the Galactic halo," Nature, vol. 477, pp. 67–69, Sept. 2011.

[35] E. Caffau, P. Bonifacio, P. François, M. Spite, F. Spite, S. Zaggia, H. G. Ludwig, M. Steffen, L. Mashonkina, L. Monaco, L. Sbordone, P. Molaro, R. Cayrel, B. Plez, V. Hill, F. Hammer, and S. Randich, "A primordial star in the heart of the Lion," A&A, vol. 542, p. A51, June 2012.

[36] D. S. Aguado, C. Allende Prieto, J. I. González Hernández, and R. Rebolo, "J0023+0307: A Mega Metal-poor Dwarf Star from SDSS/BOSS," ApJ, vol. 854, p. L34, Feb. 2018.

[37] J. Meléndez, V. M. Placco, M. Tucci-Maia, I. Ramírez, T. S. Li, and G. Perez, "2MASS J18082002-5104378: The brightest (V = 11.9) ultra metal-poor star," A&A, vol. 585, p. L5, Jan. 2016.

[38] K. C. Schlaufman, I. B. Thompson, and A. R. Casey, "An Ultra Metal-poor Star Near the Hydrogen-burning Limit," ApJ, vol. 867, p. 98, Nov. 2018.

[39] A. Frebel, "Stellar archaeology: Exploring the Universe with metal-poor stars," *Astronomische Nachrichten*, vol. 331, pp. 474–488, May 2010.

[40] A. Frebel and J. E. Norris, "Near-Field Cosmology with Extremely Metal-Poor Stars," ARA&A, vol. 53, pp. 631–688, Aug. 2015.

[41] T. Hartwig, N. Yoshida, M. Magg, A. Frebel, S. C. O. Glover, F. A. Gómez, B. Griffen, M. N. Ishigaki, A. P. Ji, R. S. Klessen, B. W. O'Shea, and N. Tominaga, "Descendants of the first stars: the distinct chemical signature of second-generation stars," MNRAS, vol. 478, pp. 1795–1810, Aug. 2018.

[42] R. Ezzeddine, A. Frebel, I. U. Roederer, N. Tominaga, J. Tumlinson, M. Ishigaki, K. Nomoto, V. M. Placco, and W. Aoki, "Evidence for an Aspherical Population III Supernova Explosion Inferred from the Hyper-metal-poor Star HE 1327-2326," ApJ, vol. 876, p. 97, May 2019.

[43] J. Alves, F. Combes, A. Ferrara, T. Forveille, and S. Shore, "Planck 2015 results," A&A, vol. 594, p. E1, Sept. 2016.

[44] A. Loeb, *How did the first stars and galaxies form?* Princeton University Press, 2010.

[45] R. Barkana and A. Loeb, "In the beginning: the first sources of light and the reionization of the universe," *Physics reports*, vol. 349, no. 2, pp. 125–238, 2001.

[46] S. Glover, *The First Stars*, vol. 396, p. 103. Springer, 2013.

[47] M. Tegmark, J. Silk, M. J. Rees, A. Blanchard, T. Abel, and F. Palla, "How Small Were the First Cosmological Objects?," ApJ, vol. 474, p. 1, Jan. 1997.

[48] T. Abel, G. L. Bryan, and M. L. Norman, "The Formation of the First Star in the Universe," *Science*, vol. 295, pp. 93–98, Jan. 2002.

[49] M. L. Norman, B. D. Smith, and J. Bordner, "Simulating the Cosmic Dawn With Enzo," *Frontiers in Astronomy and Space Sciences*, vol. 5, p. 34, Oct. 2018.

[50] V. Bromm, P. S. Coppi, and R. B. Larson, "The Formation of the First Stars. I. The Primordial Star-forming Cloud," ApJ, vol. 564, pp. 23–51, Jan. 2002.

[51] K. Omukai and F. Palla, "On the Formation of Massive Primordial Stars," ApJ, vol. 561, pp. L55–L58, Nov. 2001.

[52] N. Yoshida, K. Omukai, and L. Hernquist, "Protostar Formation in the Early Universe," *Science*, vol. 321, p. 669, Aug. 2008.

[53] A. Stacy, T. H. Greif, and V. Bromm, "The first stars: formation of binaries and small multiple systems," MNRAS, vol. 403, pp. 45–60, Mar. 2010.

[54] P. C. Clark, S. C. O. Glover, R. J. Smith, T. H. Greif, R. S. Klessen, and V. Bromm, "The Formation and Fragmentation of Disks Around Primordial Protostars," *Science*, vol. 331, p. 1040, Feb. 2011.

[55] T. H. Greif, V. Springel, S. D. M. White, S. C. O. Glover, P. C. Clark, R. J. Smith, R. S. Klessen, and V. Bromm, "Simulations on a Moving Mesh: The Clustered Formation of Population III Protostars," ApJ, vol. 737, p. 75, Aug. 2011.

[56] M. J. Turk, T. Abel, and B. O'Shea, "The Formation of Population III Binaries from Cosmological Initial Conditions," *Science*, vol. 325, p. 601, July 2009.

[57] T. Hartwig, V. Bromm, R. S. Klessen, and S. C. O. Glover, "Constraining the primordial initial mass function with stellar archaeology," MNRAS, vol. 447, pp. 3892–3908, Mar. 2015.

[58] A. Stacy, T. H. Greif, and V. Bromm, "The first stars: mass growth under protostellar feedback," MNRAS, vol. 422, pp. 290–309, May 2012.

[59] H. Susa, K. Hasegawa, and N. Tominaga, "The Mass Spectrum of the First Stars," ApJ, vol. 792, p. 32, Sept. 2014.

[60] A. Stacy, V. Bromm, and A. T. Lee, "Building up the Population III initial mass function from cosmological initial conditions," MNRAS, vol. 462, pp. 1307–1328, Oct. 2016.

[61] S. Hirano, T. Hosokawa, N. Yoshida, K. Omukai, and H. W. Yorke, "Primordial star formation under the influence of far ultraviolet radiation: 1540 cosmological haloes and the stellar mass distribution," MNRAS, vol. 448, pp. 568–587, Mar. 2015.

[62] T. Hosokawa, S. Hirano, R. Kuiper, H. W. Yorke, K. Omukai, and N. Yoshida, "Formation of Massive Primordial Stars: Intermittent UV Feedback with Episodic Mass Accretion," ApJ, vol. 824, p. 119, June 2016.

[63] D. Skinner and J. H. Wise, "Cradles of the first stars: self-shielding, halo masses, and multiplicity," MNRAS, vol. 492, pp. 4386–4397, Mar. 2020.

[64] M. J. Rees, "Opacity-limited hierarchical fragmentation and the masses of protostars," MNRAS, vol. 176, pp. 483–486, Sept. 1976.

[65] K. Omukai, "Protostellar Collapse with Various Metallicities," ApJ, vol. 534, pp. 809–824, May 2000.

[66] F. Palla, E. E. Salpeter, and S. W. Stahler, "Primordial star formation - The role of molecular hydrogen," ApJ, vol. 271, pp. 632–641, Aug. 1983.

[67] K. Omukai and R. Nishi, "Formation of Primordial Protostars," ApJ, vol. 508, pp. 141–150, Nov. 1998.

[68] F. H. Shu, "Self-similar collapse of isothermal spheres and star formation.," ApJ, vol. 214, pp. 488–497, June 1977.

[69] V. Bromm and R. B. Larson, "The First Stars," ARA&A, vol. 42, pp. 79–118, Sept. 2004.

[70] T. H. Greif, V. Bromm, P. C. Clark, S. C. O. Glover, R. J. Smith, R. S. Klessen, N. Yoshida, and V. Springel, "Formation and evolution of primordial protostellar systems," MNRAS, vol. 424, pp. 399–415, July 2012.

[71] N. Yoshida, T. Abel, L. Hernquist, and N. Sugiyama, "Simulations of Early Structure Formation: Primordial Gas Clouds," ApJ, vol. 592, pp. 645–663, Aug. 2003.

[72] L. Gao, S. D. M. White, A. Jenkins, C. S. Frenk, and V. Springel, "Early structure in ΛCDM," MNRAS, vol. 363, pp. 379–392, Oct. 2005.

[73] N. Yoshida, K. Omukai, L. Hernquist, and T. Abel, "Formation of Primordial Stars in a ΛCDM Universe," ApJ, vol. 652, pp. 6–25, Nov. 2006.

[74] S. Glover, "The Formation Of The First Stars In The Universe," Space Sci. Rev., vol. 117, pp. 445–508, Apr. 2005.

[75] V. Bromm, N. Yoshida, L. Hernquist, and C. F. McKee, "The formation of the first stars and galaxies," *Nature*, vol. 459, no. 7243, pp. 49–54, 2009.

[76] Z. Haiman, A. A. Thoul, and A. Loeb, "Cosmological Formation of Low-Mass Objects," ApJ, vol. 464, p. 523, June 1996.

[77] I. D. McGreer and G. L. Bryan, "HD Cooling in Primordial Star Formation," in *First Stars III* (B. W. O'Shea and A. Heger, eds.), vol. 990 of *American Institute of Physics Conference Series*, pp. 30–32, Mar. 2008.

[78] T. H. Greif, V. Springel, and V. Bromm, "On the operation of the chemothermal instability in primordial star-forming clouds," MNRAS, vol. 434, pp. 3408–3422, Oct. 2013.

[79] S. Glover, "Chemistry and Cooling in Metal-Free and Metal-Poor Gas," in *First Stars III* (B. W. O'Shea and A. Heger, eds.), vol. 990 of *American Institute of Physics Conference Series*, pp. 25–29, Mar. 2008.

[80] E. Ripamonti, F. Haardt, A. Ferrara, and M. Colpi, "Radiation from the first forming stars," MNRAS, vol. 334, pp. 401–418, Aug. 2002.

[81] P. C. Clark, S. C. O. Glover, R. J. Smith, T. H. Greif, R. S. Klessen, and V. Bromm, "The Formation and Fragmentation of Disks Around Primordial Protostars," *Science*, vol. 331, p. 1040, Feb. 2011.

[82] T. H. Greif, V. Springel, S. D. M. White, S. C. O. Glover, P. C. Clark, R. J. Smith, R. S. Klessen, and V. Bromm, "Simulations on a Moving Mesh: The Clustered Formation of Population III Protostars," ApJ, vol. 737, p. 75, Aug. 2011.

[83] T. Hartwig, P. C. Clark, S. C. O. Glover, R. S. Klessen, and M. Sasaki, "A New Approach to Determine Optically Thick H_2 Cooling and its Effect on Primordial Star Formation," ApJ, vol. 799, p. 114, Feb. 2015.

[84] L. Frommhold, *Collision-induced Absorption in Gases*. NRC Research Press Ottawa, Canada, 1994.

[85] E. Ripamonti and T. Abel, "Fragmentation and the formation of primordial protostars: the possible role of collision-induced emission," MNRAS, vol. 348, pp. 1019–1034, Mar. 2004.

[86] R. B. Larson, "Numerical calculations of the dynamics of collapsing proto-star," MNRAS, vol. 145, p. 271, Jan. 1969.

[87] M. V. Penston, "Dynamics of self-gravitating gaseous spheres-III. Analyt-ical results in the free-fall of isothermal cases," MNRAS, vol. 144, p. 425, Jan. 1969.

[88] J. C. Tan and E. G. Blackman, "Protostellar Disk Dynamos and Hydromag-netic Outflows in Primordial Star Formation," ApJ, vol. 603, pp. 401–413, Mar. 2004.

[89] A. Stacy, C. F. McKee, A. T. Lee, R. I. Klein, and P. S. Li, "Magnetic fields in the formation of the first stars - II. Results," MNRAS, vol. 511, pp. 5042–5069, Apr. 2022.

[90] S. W. Stahler, F. Palla, and E. E. Salpeter, "Primordial Stellar Evolution: The Protostar Phase," ApJ, vol. 302, p. 590, Mar. 1986.

[91] P. P. Kronberg, "Extragalactic magnetic fields," *Reports on Progress in Physics*, vol. 57, pp. 325–382, Apr. 1994.

[92] L. M. Widrow, D. Ryu, D. R. G. Schleicher, K. Subramanian, C. G. Tsagas, and R. A. Treumann, "The First Magnetic Fields," Space Sci. Rev., vol. 166, pp. 37–70, May 2012.

[93] H. Katz, S. Martin-Alvarez, J. Devriendt, A. Slyz, and T. Kimm, "Magne-togenesis at Cosmic Dawn: tracing the origins of cosmic magnetic fields," MNRAS, vol. 484, pp. 2620–2631, Apr. 2019.

[94] A. Reiners, "Observations of cool-star magnetic fields," *Living Reviews in Solar Physics*, vol. 9, no. 1, pp. 1–73, 2012.

[95] M. D. Johnson, V. L. Fish, S. S. Doeleman, D. P. Marrone, R. L. Plambeck, J. F. Wardle, K. Akiyama, K. Asada, C. Beaudoin, L. Blackburn, *et al.*, "Resolved magnetic-field structure and variability near the event horizon of sagittarius a," *Science*, vol. 350, no. 6265, pp. 1242–1245, 2015.

[96] D. D. Mulcahy, A. Horneffer, R. Beck, G. Heald, A. Fletcher, A. Scaife, B. Adebahr, J. M. Anderson, A. Bonafede, M. Brüggen, G. Brunetti, K. T. Chyży, J. Conway, R. J. Dettmar, T. Enßlin, M. Haverkorn, C. Horellou, M. Iacobelli, F. P. Israel, H. Junklewitz, W. Jurusik, J. Köhler, M. Ku-niyoshi, E. Orrú, R. Paladino, R. Pizzo, W. Reich, and H. J. A. Röttgering, "The nature of the low-frequency emission of M 51. First observations of a nearby galaxy with LOFAR," A&A, vol. 568, p. A74, Aug. 2014.

[97] F. Govoni and L. Feretti, "Magnetic Fields in Clusters of Galaxies," *Inter-national Journal of Modern Physics D*, vol. 13, pp. 1549–1594, Jan. 2004.

[98] D. Grasso and H. R. Rubinstein, "Magnetic fields in the early Universe," Phys. Rep., vol. 348, pp. 163–266, July 2001.

[99] M. L. Bernet, F. Miniati, S. J. Lilly, P. P. Kronberg, and M. Dessauges-Zavadsky, "Strong magnetic fields in normal galaxies at high redshift," Nature, vol. 454, pp. 302–304, July 2008.

[100] A. Neronov and I. Vovk, "Evidence for Strong Extragalactic Magnetic Fields from Fermi Observations of TeV Blazars," *Science*, vol. 328, p. 73, Apr. 2010.

[101] F. Tavecchio, G. Ghisellini, L. Foschini, G. Bonnoli, G. Ghirlanda, and P. Coppi, "The intergalactic magnetic field constrained by Fermi/Large Area Telescope observations of the TeV blazar 1ES0229+200," MNRAS, vol. 406, pp. L70–L74, July 2010.

[102] K. Dolag, M. Kachelriess, S. Ostapchenko, and R. Tomàs, "Lower Limit on the Strength and Filling Factor of Extragalactic Magnetic Fields," ApJ, vol. 727, p. L4, Jan. 2011.

[103] A. M. Beck, M. Hanasz, H. Lesch, R. S. Remus, and F. A. Stasyszyn, "On the magnetic fields in voids.," MNRAS, vol. 429, pp. L60–L64, Feb. 2013.

[104] P. Blasi, S. Burles, and A. V. Olinto, "Cosmological Magnetic Field Limits in an Inhomogeneous Universe," ApJ, vol. 514, pp. L79–L82, Apr. 1999.

[105] J. P. Vallée, "Cosmic magnetic fields - as observed in the Universe, in galactic dynamos, and in the Milky Way," New A Rev., vol. 48, pp. 763–841, Sept. 2004.

[106] J. D. Barrow, P. G. Ferreira, and J. Silk, "Constraints on a Primordial Magnetic Field," Phys. Rev. Lett., vol. 78, pp. 3610–3613, May 1997.

[107] T. R. Seshadri and K. Subramanian, "Cosmic Microwave Background Bispectrum from Primordial Magnetic Fields on Large Angular Scales," Phys. Rev. Lett., vol. 103, p. 081303, Aug. 2009.

[108] Planck Collaboration, "Planck 2015 results. XIX. Constraints on primordial magnetic fields," A&A, vol. 594, p. A19, Sept. 2016.

[109] D. Paoletti and F. Finelli, "Constraints on primordial magnetic fields from magnetically-induced perturbations: current status and future perspectives with LiteBIRD and future ground based experiments," J. Cosmology Astropart. Phys., vol. 2019, p. 028, Nov. 2019.

[110] K. Dolag, M. Bartelmann, and H. Lesch, "SPH simulations of magnetic fields in galaxy clusters," A&A, vol. 348, pp. 351–363, Aug. 1999.

[111] K. Dolag, D. Grasso, V. Springel, and I. Tkachev, "Constrained simulations of the magnetic field in the local Universe and the propagation of ultrahigh energy cosmic rays," J. Cosmology Astropart. Phys., vol. 2005, p. 009, Jan. 2005.

[112] D. G. Yamazaki, K. Ichiki, T. Kajino, and G. J. Mathews, "New constraints on the primordial magnetic field," Phys. Rev. D, vol. 81, p. 023008, Jan. 2010.

[113] D. Paoletti, J. Chluba, F. Finelli, and J. A. Rubiño-Martin, "Constraints on Primordial Magnetic Fields from their impact on the ionization history with Planck 2018," arXiv e-prints, p. arXiv:2204.06302, Apr. 2022.

[114] L. Pogosian and A. Zucca, "Searching for primordial magnetic fields with CMB B-modes," Classical and Quantum Gravity, vol. 35, p. 124004, June 2018.

[115] A. Kandus, K. E. Kunze, and C. G. Tsagas, "Primordial magnetogenesis," Physics Reports, vol. 505, p. 1–58, Aug 2011.

[116] K. Subramanian, "The origin, evolution and signatures of primordial magnetic fields," Reports on Progress in Physics, vol. 79, p. 076901, May 2016.

[117] K. Jedamzik and L. Pogosian, "Relieving the Hubble Tension with Primordial Magnetic Fields," Phys. Rev. Lett., vol. 125, p. 181302, Oct. 2020.

[118] K. Jedamzik and T. Abel, "Weak Primordial Magnetic Fields and Anisotropies in the Cosmic Microwave Background Radiation," arXiv e-prints, p. arXiv:1108.2517, Aug. 2011.

[119] K. Jedamzik and A. Saveliev, "Stringent Limit on Primordial Magnetic Fields from the Cosmic Microwave Background Radiation," Phys. Rev. Lett., vol. 123, p. 021301, July 2019.

[120] D. G. Yamazaki, T. Kajino, G. J. Mathews, and K. Ichiki, "The search for a primordial magnetic field," Phys. Rep., vol. 517, pp. 141–167, Aug. 2012.

[121] A. Mack, T. Kahniashvili, and A. Kosowsky, "Microwave background signatures of a primordial stochastic magnetic field," Phys. Rev. D, vol. 65, p. 123004, June 2002.

[122] E. R. Harrison, "Generation of magnetic fields in the radiation ERA," MN-RAS, vol. 147, p. 279, Jan. 1970.

[123] R. Banerjee and K. Jedamzik, "Are Cluster Magnetic Fields Primordial?," Phys. Rev. Lett., vol. 91, p. 251301, Dec. 2003.

[124] M. S. Turner and L. M. Widrow, "Inflation-produced, large-scale magnetic fields," Phys. Rev. D, vol. 37, pp. 2743–2754, May 1988.

[125] J. M. Quashnock, A. Loeb, and D. N. Spergel, "Magnetic Field Generation during the Cosmological QCD Phase Transition," ApJ, vol. 344, p. L49, Sept. 1989.

[126] S. A. Bonometto and O. Pantano, "Physics of the cosmological quark-hadron transition.," Phys. Rep., vol. 228, pp. 175–252, June 1993.

[127] G. Baym, D. Bödeker, and L. McLerran, "Magnetic fields produced by phase transition bubbles in the electroweak phase transition," Phys. Rev. D, vol. 53, pp. 662–667, Jan. 1996.

[128] K. Ichiki, K. Takahashi, H. Ohno, H. Hanayama, and N. Sugiyama, "Cosmological Magnetic Field: A Fossil of Density Perturbations in the Early Universe," *Science*, vol. 311, pp. 827–829, Feb. 2006.

[129] L. Biermann, "Über den Ursprung der Magnetfelder auf Sternen und im interstellaren Raum (miteinem Anhang von A. Schlüter)," *Zeitschrift Naturforschung Teil A*, vol. 5, p. 65, Jan. 1950.

[130] H. Xu, B. W. O'Shea, D. C. Collins, M. L. Norman, H. Li, and S. Li, "The Biermann Battery in Cosmological MHD Simulations of Population III Star Formation," ApJ, vol. 688, p. L57, Dec. 2008.

[131] M. Lazar, R. Schlickeiser, R. Wielebinski, and S. Poedts, "Cosmological Effects of Weibel-Type Instabilities," ApJ, vol. 693, pp. 1133–1141, Mar. 2009.

[132] M. V. Medvedev, L. O. Silva, M. Fiore, R. A. Fonseca, and W. B. Mori, "Generation of Magnetic Fields in Cosmological Shocks," *Journal of Korean Astronomical Society*, vol. 37, pp. 533–541, Dec. 2004.

[133] R. Schlickeiser and P. K. Shukla, "Cosmological Magnetic Field Generation by the Weibel Instability," ApJ, vol. 599, pp. L57–L60, Dec. 2003.

[134] R. Banerjee and K. Jedamzik, "Evolution of cosmic magnetic fields: From the very early Universe, to recombination, to the present," Phys. Rev. D, vol. 70, p. 123003, Dec. 2004.

[135] R. M. Kulsrud, R. Cen, J. P. Ostriker, and D. Ryu, "The Protogalactic Origin for Cosmic Magnetic Fields," ApJ, vol. 480, pp. 481–491, May 1997.

[136] J. Schober, D. Schleicher, C. Federrath, S. Glover, R. S. Klessen, and R. Banerjee, "The Small-scale Dynamo and Non-ideal Magnetohydrodynamics in Primordial Star Formation," ApJ, vol. 754, p. 99, Aug. 2012.

[137] C. F. McKee, A. Stacy, and P. S. Li, "Magnetic Fields in the Formation of the First Stars. I. Theory vs. Simulation," MNRAS, July 2020.

[138] A. P. Kazantsev, "Enhancement of a Magnetic Field by a Conducting Fluid," *Soviet Journal of Experimental and Theoretical Physics*, vol. 26, p. 1031, May 1968.

[139] K. Subramanian, "Can the turbulent galactic dynamo generate large-scale magnetic fields?," MNRAS, vol. 294, pp. 718–728, Mar. 1998.

[140] J. Schober, D. Schleicher, C. Federrath, R. Klessen, and R. Banerjee, "Magnetic field amplification by small-scale dynamo action: Dependence on turbulence models and Reynolds and Prandtl numbers," Phys. Rev. E, vol. 85, p. 026303, Feb. 2012.

[141] J. Schober, D. R. G. Schleicher, C. Federrath, S. Bovino, and R. S. Klessen, "Saturation of the turbulent dynamo," Phys. Rev. E, vol. 92, p. 023010, Aug. 2015.

[142] C. Federrath, S. Sur, D. R. G. Schleicher, R. Banerjee, and R. S. Klessen, "A New Jeans Resolution Criterion for (M)HD Simulations of Self-gravitating Gas: Application to Magnetic Field Amplification by Gravity-driven Turbulence," ApJ, vol. 731, p. 62, Apr. 2011.

[143] C. Federrath, J. Schober, S. Bovino, and D. R. G. Schleicher, "The Turbulent Dynamo in Highly Compressible Supersonic Plasmas," ApJ, vol. 797, p. L19, Dec. 2014.

[144] P. Sharda, C. Federrath, and M. R. Krumholz, "The importance of magnetic fields for the initial mass function of the first stars," MNRAS, vol. 497, pp. 336–351, Sept. 2020.

[145] T. Vachaspati, "Progress on cosmological magnetic fields," *Reports on Progress in Physics*, vol. 84, p. 074901, July 2021.

[146] K. Subramanian, D. Narasimha, and S. M. Chitre, "Thermal generation of cosmological seed magnetic fields in ionization fronts," MNRAS, vol. 271, p. L15, Nov. 1994.

[147] J. Wurster and Z.-Y. Li, "The role of magnetic fields in the formation of protostellar discs," *Frontiers in Astronomy and Space Sciences*, vol. 5, p. 39, Dec. 2018.

[148] R. Teyssier and B. Commerçon, "Numerical Methods for Simulating Star Formation," *Frontiers in Astronomy and Space Sciences*, vol. 6, p. 51, July 2019.

[149] P. Hennebelle and S.-i. Inutsuka, "The role of magnetic field in molecular cloud formation and evolution," *Frontiers in Astronomy and Space Sciences*, vol. 6, p. 5, Mar. 2019.

[150] B. Zhao, K. Tomida, P. Hennebelle, J. J. Tobin, A. Maury, T. Hirota, Á. Sánchez-Monge, R. Kuiper, A. Rosen, A. Bhandare, M. Padovani, and Y.-N. Lee, "Formation and Evolution of Disks Around Young Stellar Objects," Space Sci. Rev., vol. 216, p. 43, Apr. 2020.

[151] M. N. Machida, T. Matsumoto, and S.-i. Inutsuka, "Magnetohydrodynamics of Population III Star Formation," ApJ, vol. 685, pp. 690–704, Oct. 2008.

[152] D. R. G. Schleicher, D. Galli, S. C. O. Glover, R. Banerjee, F. Palla, R. Schneider, and R. S. Klessen, "The Influence of Magnetic Fields on the Thermodynamics of Primordial Star Formation," ApJ, vol. 703, pp. 1096–1106, Sept. 2009.

[153] D. R. G. Schleicher, R. Banerjee, S. Sur, T. G. Arshakian, R. S. Klessen, R. Beck, and M. Spaans, "Small-scale dynamo action during the formation of the first stars and galaxies. I. The ideal MHD limit," A&A, vol. 522, p. A115, Nov. 2010.

[154] S. Sur, D. R. G. Schleicher, R. Banerjee, C. Federrath, and R. S. Klessen, "The Generation of Strong Magnetic Fields During the Formation of the First Stars," ApJ, vol. 721, pp. L134–L138, Oct. 2010.

[155] M. A. Latif, D. R. G. Schleicher, W. Schmidt, and J. Niemeyer, "The small-scale dynamo and the amplification of magnetic fields in massive primordial haloes," MNRAS, vol. 432, pp. 668–678, June 2013.

[156] M. N. Machida and K. Doi, "The formation of Population III stars in gas accretion stage: effects of magnetic fields," MNRAS, vol. 435, pp. 3283–3305, Nov. 2013.

[157] M. A. Latif and D. R. G. Schleicher, "Magnetic fields in primordial accretion disks," A&A, vol. 585, p. A151, Jan. 2016.

[158] S. Hirano and V. Bromm, "Formation and survival of Population III stellar systems," MNRAS, vol. 470, pp. 898–914, Sept. 2017.

[159] P. Grete, M. A. Latif, D. R. G. Schleicher, and W. Schmidt, "Intermittent fragmentation and statistical variations during gas collapse in magnetized atomic cooling haloes," MNRAS, vol. 487, pp. 4525–4535, Aug. 2019.

[160] P. Sharda, C. Federrath, M. R. Krumholz, and D. R. G. Schleicher, "Magnetic field amplification in accretion discs around the first stars: implications for the primordial IMF," *arXiv e-prints*, p. arXiv:2007.02678, July 2020.

[161] D. Koh, T. Abel, and K. Jedamzik, "First Star Formation in the Presence of Primordial Magnetic Fields," ApJ, vol. 909, p. L21, Mar. 2021.

[162] E. Garaldi, R. Pakmor, and V. Springel, "Magnetogenesis around the first galaxies: the impact of different field seeding processes on galaxy formation," MNRAS, vol. 502, pp. 5726–5744, Apr. 2021.

[163] K. E. Sadanari, K. Omukai, K. Sugimura, T. Matsumoto, and K. Tomida, "Magnetohydrodynamic effect on first star formation: prestellar core collapse and protostar formation," MNRAS, May 2021.

[164] R. Banerjee, S. Sur, C. Federrath, D. R. G. Schleicher, and R. S. Klessen, "Generation of strong magnetic fields via the small-scale dynamo during the formation of the first stars," *arXiv e-prints*, p. arXiv:1202.4536, Feb. 2012.

[165] M. N. Machida, S.-i. Inutsuka, and T. Matsumoto, "Second Core Formation and High-Speed Jets: Resistive Magnetohydrodynamic Nested Grid Simulations," ApJ, vol. 647, pp. L151–L154, Aug. 2006.

[166] S. Sur, C. Federrath, D. R. G. Schleicher, R. Banerjee, and R. S. Klessen, "Magnetic field amplification during gravitational collapse - influence of turbulence, rotation and gravitational compression," MNRAS, vol. 423, pp. 3148–3162, July 2012.

[167] C. Federrath, J. Roman-Duval, R. S. Klessen, W. Schmidt, and M. M. Mac Low, "Comparing the statistics of interstellar turbulence in simulations and observations. Solenoidal versus compressive turbulence forcing," A&A, vol. 512, p. A81, Mar. 2010.

[168] M. N. Ishigaki, N. Tominaga, C. Kobayashi, and K. Nomoto, "The Initial Mass Function of the First Stars Inferred from Extremely Metal-poor Stars," ApJ, vol. 857, p. 46, Apr. 2018.

[169] N. E. Haugen, A. Brandenburg, and W. Dobler, "Simulations of nonhelical hydromagnetic turbulence," Phys. Rev. E, vol. 70, p. 016308, July 2004.

[170] C. Federrath, G. Chabrier, J. Schober, R. Banerjee, R. S. Klessen, and D. R. G. Schleicher, "Mach Number Dependence of Turbulent Magnetic Field Amplification: Solenoidal versus Compressive Flows," Phys. Rev. Lett., vol. 107, p. 114504, Sept. 2011.

[171] A. Brandenburg, "Magnetic Prandtl Number Dependence of the Kinetic-to-magnetic Dissipation Ratio," ApJ, vol. 791, p. 12, Aug. 2014.

[172] S. Xu and A. Lazarian, "Turbulent Dynamo in a Conducting Fluid and a Partially Ionized Gas," ApJ, vol. 833, p. 215, Dec. 2016.

[173] M. A. Latif, D. R. G. Schleicher, and W. Schmidt, "Magnetic fields during the formation of supermassive black holes," MNRAS, vol. 440, pp. 1551–1561, May 2014.

[174] G. L. Bryan, M. L. Norman, B. W. O'Shea, T. Abel, J. H. Wise, M. J. Turk, D. R. Reynolds, D. C. Collins, P. Wang, S. W. Skillman, *et al.*, "Enzo: An adaptive mesh refinement code for astrophysics," *The Astrophysical Journal Supplement Series*, vol. 211, no. 2, p. 19, 2014.

[175] O. Hahn and T. Abel, "MUSIC: MUlti-Scale Initial Conditions," *Astrophysics Source Code Library*, pp. ascl–1311, 2013.

[176] B. D. Smith, G. L. Bryan, S. C. O. Glover, N. J. Goldbaum, M. J. Turk, J. Regan, J. H. Wise, H.-Y. Schive, T. Abel, A. Emerick, B. W. O'Shea, P. Anninos, C. B. Hummels, and S. Khochfar, "GRACKLE: a chemistry and cooling library for astrophysics," MNRAS, vol. 466, pp. 2217–2234, Apr. 2017.

[177] M. J. Turk, P. Clark, S. C. O. Glover, T. H. Greif, T. Abel, R. Klessen, and V. Bromm, "Effects of Varying the Three-body Molecular Hydrogen Formation Rate in Primordial Star Formation," ApJ, vol. 726, p. 55, Jan. 2011.

[178] P. Anninos, Y. Zhang, T. Abel, and M. L. Norman, "Cosmological hydrodynamics with multi-species chemistry and nonequilibrium ionization and cooling," New A, vol. 2, pp. 209–224, Aug. 1997.

[179] K. Omukai and F. Palla, "Formation of the First Stars by Accretion," ApJ, vol. 589, pp. 677–687, June 2003.

[180] T. H. Greif, "The numerical frontier of the high-redshift Universe," *Computational Astrophysics and Cosmology*, vol. 2, p. 3, Mar. 2015.

[181] C. Safranek-Shrader, M. H. Montgomery, M. Milosavljević, and V. Bromm, "Star formation in the first galaxies - III. Formation, evolution, and characteristics of the first metal-enriched stellar cluster," MNRAS, vol. 455, pp. 3288–3302, Jan. 2016.

[182] A. Stacy, T. H. Greif, R. S. Klessen, V. Bromm, and A. Loeb, "Rotation and internal structure of Population III protostars," MNRAS, vol. 431, pp. 1470–1486, May 2013.

[183] P. Colella and P. R. Woodward, "The Piecewise Parabolic Method (PPM) for Gas-Dynamical Simulations," *Journal of Computational Physics*, vol. 54, pp. 174–201, Sept. 1984.

[184] E. F. Toro, *Riemann solvers and numerical methods for fluid dynamics: a practical introduction*. Springer Science & Business Media, 2013.

[185] A. Dedner, F. Kemm, D. Kröner, C. D. Munz, T. Schnitzer, and M. Wesenberg, "Hyperbolic Divergence Cleaning for the MHD Equations," *Journal of Computational Physics*, vol. 175, pp. 645–673, Jan. 2002.

[186] C. Safranek-Shrader, M. Agarwal, C. Federrath, A. Dubey, M. Milosavljević, and V. Bromm, "Star formation in the first galaxies - I. Collapse delayed by Lyman-Werner radiation," MNRAS, vol. 426, pp. 1159–1177, Oct. 2012.

[187] S. Hirano and V. Bromm, "Angular momentum transfer in primordial discs and the rotation of the first stars," MNRAS, vol. 476, pp. 3964–3973, May 2018.

[188] C. R. Saad, V. Bromm, and M. El Eid, "Impact of magnetic fields on Population III star formation," MNRAS, vol. 516, pp. 3130–3143, Nov. 2022.

[189] A. Toomre, "On the gravitational stability of a disk of stars.," ApJ, vol. 139, pp. 1217–1238, May 1964.

[190] B. D. Smith, M. J. Turk, S. Sigurdsson, B. W. O'Shea, and M. L. Norman, "Three Modes of Metal-Enriched Star Formation in the Early Universe," ApJ, vol. 691, pp. 441–451, Jan. 2009.

[191] D. Nakauchi, K. Omukai, and H. Susa, "Ionization degree and magnetic diffusivity in the primordial star-forming clouds," MNRAS, vol. 488, pp. 1846–1862, Sept. 2019.